Heliyon 10 (2024) e23517

Contents lists available at ScienceDirect

Heliyon

journal homepage: www.cell.com/heliyon

Highly crystalline and fluorescent BODIPY-labelled phenyl-triazole-coumarins as *n*-type semiconducting materials for OFET devices

José Emilio de la Cerda-Pedro [a], Oscar Javier Hernández-Ortiz [a,b], Rosa Angeles Vázquez-García [b], Efrén V. García-Báez [a], Ramón Gómez-Aguilar [c], Arián Espinosa-Roa [d], Norberto Farfán [e], Itzia I. Padilla-Martínez [a,*]

[a] *Laboratorio de Química Supramolecular y Nanociencias de la Unidad Profesional Interdisciplinaria de Biotecnología del Instituto Politécnico Nacional, Av. Acueducto s/n Barrio la laguna Ticomán, 07340, Ciudad de Mexico, Mexico*
[b] *Área Académica de Ciencias de la Tierra y Materiales, Universidad Autónoma del Estado de Hidalgo, km. 4.5 Carretera Pachuca-Tulancingo, Col. Carboneras 42184, Mineral de la Reforma, Hidalgo Mexico*
[c] *Unidad Profesional en Ingeniería y Tecnologías Avanzadas del Instituto Politécnico Nacional, Av. I.P.N No. 2580 Col. La Laguna Ticomán, Gustavo A. Madero 07340, Ciudad de Mexico, Mexico*
[d] *CONAHCYT-Centro de Investigación en Química Aplicada Unidad Monterrey, Sur 204 Parque de Innovación e Investigación Tecnológica, Km. 10 autopista al Aeropuerto Internacional Mariano Escobedo, 66628, Apodaca, Nuevo Leon, Mexico*
[e] *Departamento de Química Orgánica, Facultad de Química, Universidad Nacional Autónoma de México, Circuito Escolar, Ciudad Universitaria 04510, Ciudad de Mexico, Mexico*

ARTICLE INFO

Keywords:
Phenyl-triazole
OFET
BODIPY
Organic semiconductor
Organic small molecule devices
Organic field-effect transistors

ABSTRACT

In this work, the synthesis of BODIPY-phenyl-triazole labelled coumarins (BPhTCs) using a two-step approach is described. The influence of the BODIPY appending on the photophysical, electrochemical and thermal properties of the phenyl-triazole-coumarin precursors (PhTCs) was investigated. Band gap energies were measured by absorption spectroscopy (2.20 ± 0.02 eV in the solid and 2.35 ± 0.01 eV in solution) and cyclic voltammetry (2.10 ± 0.05 eV). The results are supported by DFT calculations confirming the presence of lowest LUMO levels that facilitate the electron injection and stabilize the electron transport. Their charge-transport parameters were measured in Organic Field-Effect Transistor (OFET) devices. BPhTCs showed an ambipolar transistor behavior with good n-type charge mobilities (10^{-2} $cm^2V^{-1}s^{-1}$) allowing these derivatives to be employed as promising semiconducting crystalline and fluorescent materials with good thermal and air stability up to 250 °C.

1. Introduction

BODIPY derivatives, acronym of boron-dipyrromethene (4,4-difluoro-4-bora-3*a*,4*a*-diaza-*s*-indacene), have lately attracted wide research interest due to their remarkable photophysical properties: absorption-emission bands in the near UV–vis region, high fluorescence quantum yields (Φ_f) with an average lifetime between 1 and 10 ns, important molar absorption coefficients, and distinctive photochemical stability [1–3]. Consequently, the BODIPY unit has recently found potential application in a wide variety of fields such

* Corresponding author.
E-mail address: ipadillamar@ipn.mx (I.I. Padilla-Martínez).

https://doi.org/10.1016/j.heliyon.2023.e23517
Received 14 August 2023; Received in revised form 4 December 2023; Accepted 5 December 2023
Available online 10 December 2023

as laser technology, solar cell industry [4–7], bioimaging acquisition [8–10], photodynamic therapy [11,12], viscosity measurements [13,14], chemosensors [15], and electroluminescent devices [16], among other applications. BODIPY derivatives constitute a new generation of outstanding functional materials with characteristics suitable to be used as organic semiconductor (OS) materials [17–19]. They show mechanical flexibility and good charge mobilities (10^{-5}-10^{-2} $cm^2V^{-1}s^{-1}$) [5,20]. In the last decade, there has been a growing interest to develop BODIPY derivatives for optoelectronic applications [21], most of them focused on polymers. In this regard, a copolymer conjugated with thiophene-substituted BODIPY [22] is considered as the OS-BODIPY with the highest charge mobility (0.17 $cm^2V^{-1}s^{-1}$). As far as BODIPY-based small molecules for OTFTs are concerned, their development has been more limited but with results equivalent to BODIPY-polymeric materials (0.01 $cm^2V^{-1}s^{-1}$) [23].

The optical and electronic properties of BODIPYs are mostly relied on the type of substituent and the position at which they are attached (*meso*, α and β). Therefore, the BODIPY has been coupled to other derivatives with intrinsic biological or optical properties to increase scope for synergy. In this sense, coumarin compounds show high fluorescence quantum yields and stability under UV light [24]. Push-pull arrangement is developed in the coumarin system, through the combination of electron-withdrawing (EW) and electron-donor (ED) substituents on C-3 and C-7, respectively. The strong polarization of this combination of opposites allows tuning of their absorption-emission profiles [25]. Then, BODIPY-coumarin hybrids (BC) exhibit large bathochromic and Stokes shifts with improved quantum yields [26–28]. Besides, α,β−unsaturated compounds [29,30], amides [31], indole derivatives [32], phenyl [33], carbazole [34], and thiophene derivatives [35] have been used to link BODIPY and coumarin fluorophores to achieve specific properties.

On the other hand, BODIPY-triazole hybrids (BT) are recognized because of their rigidity, aromaticity, high chemical stability, and polarity as well as their capability of hydrogen bonding association [36]. The enhanced photo-physical properties of BT hybrids allowed their application as Hg^{2+}, Ag^{+} and human leukocyte elastase fluorescent chemosensors [37–40], for light harvesting [41], and *in vitro* labelling of cells and glycoproteins [42].

In addition, hybrids of triazole-coumarin moieties (TC) exhibit improved optical properties which can be modulated by the electronic nature and position on the coumarin substituents [43–45]. TC bifunctional hybrids have been applied as fluorescent sensors of physiological H_2O_2, H_2S, Cu^{2+}, Pd^{2+}, as well as a probe for HNO in living cells [46–50].

In addition, hybrids of triazole-coumarin moieties (TC) are known to exhibit improved optical properties tuned by the electronic nature and position on the coumarin substituents [43–45]. TC bifunctional hybrids have been applied as fluorescent sensors of physiological H_2O_2, H_2S, Cu^{2+}, Pd^{2+}, as well as a probe for HNO in living cells [46–50].

One approach to the novel materials is a combination of known luminophores, then and based on the improved above mentioned photophysical properties of BC, BT and TC hybrids, herein the 1,2,3-triazolyl-phenyl moiety (PhT), as donor (D), is used to connect the BODIPY (B) and coumarin (C) fragments, as the acceptors. Thus A–D dyads were prepared by modulating the acceptor nature of the coumarin unit with the appropriate substituent. Previously, we reported the synthesis, of the precursors 3-(4-formylphenyl)-triazole-coumarins and demonstrated their suitability for optoelectronic applications [51]. Taking advantage of the availability of the starting materials, BODIPY-1,2,3-triazolyl-phenyl-coumarin (BPhTC) hybrids **2a-g**, Fig. 1, were herein prepared for the first time. The strong ED substituents (NEt_2, OR (R═H, Me, Et)) and those EDs with negative inductive effect (Cl, Br), in positions 6–8 on the coumarin ring, offer the possibility to relate them with optoelectronic properties. It is worth mentioning that the combination of these three heterocycles, has not been reported before neither as luminophores nor as OS materials. The BPhTCs hybrid materials, **2a-g**, are *meso*-substituted BODIPYs, this substitution is expected to lead to n-channel semiconducting characteristics [21], less frequently studied than the p-channel transistor behavior of small molecule OS materials.

The synthesis of BPhTC-hybrids **2a-g** was performed in two steps. They were spectroscopically, spectrometric, thermally, and electrochemically characterized, and their crystalline nature was established by X-ray diffraction. Furthermore, their photophysical properties, in solution and the solid state, were explored and supported by mechano-quantum calculations (DFT). Finally, films of BPhTCs were characterized by atomic force microscopy and their characteristics as OS materials were tested using organic field-effect

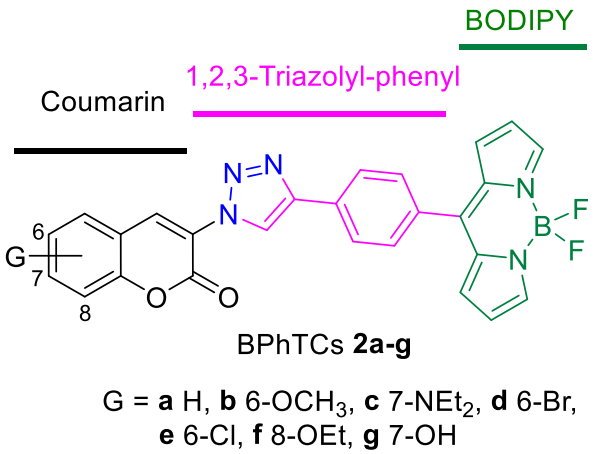

Fig. 1. BODIPY-1,2,3-triazolyl-phenyl-coumarin (BPhTC) hybrids **2a-g.**

transistor (OFET) devices as micro-labs. BPhTCs showed to be crystalline materials with good thermal and air stability suitable as luminophores and OS with good n-type charge mobilities.

2. Materials and methods

All reagents were purchased from Sigma-Aldrich. Aldehydes **1a-g** were synthesized as reported [51]. Structural characterization of **1a-g** is given in the supplementary material (S1). Standard procedures were followed to dry the organic solvents. Column chromatography was performed using standard silica gel 60. Melting points were determined with an Electrothermal AI 9100 apparatus or a Büchi Melting Point B540 and are uncorrected. FT-IR spectra were recorded on a PerkinElmer Spectrum GX Spectrophotometer and are reported as wavenumber of absorption (cm^{-1}). ^{1}H, ^{13}C, ^{11}B and ^{19}F NMR spectra were acquired on Varian NMR spectrometers, operating at 300 and 400 MHz, and on Bruker NMR spectrometer Avance III, operating a 750 MHz, using DMSO-d_6 as solvent unless otherwise is specified. Chemical shifts (δ) are reported in parts per million (ppm) from the residual solvent peak used as reference and coupling constants (^{n}J) are in Hz. The following abbreviations are used to indicate the multiplicity of the signals: s, singlet (s); d, doublet; t, triplet; q, quadruplet; m, multiplet. Agilent G1969A spectrometer was used to obtain high resolution mass spectra.

2.1. General procedure for the synthesis of BODIPY-1,2,3-triazolyl-phenyl-coumarin hybrids (BPhTCs 2a-g), and their characterization

Compounds **2a-g** were prepared according to conventional two-step one pot procedure for BODIPYs synthesis [7,52,53] with modifications. A detailed protocol is described in the supplementary material (S2). NMR and HR-MS spectra can be found in the supplementary material (S3).

meso-(4-(1-(2-oxo-2*H*-chromen-3-yl)-1*H*-1,2,3-triazol-4-yl))phenyl-4,4-difluoro-4-bora-3*a*,4*a*-diaza-*s*-indacene (**2a**).

Orange crystalline solid (60 %). Mp: 281–283 °C. ^{1}H NMR (300 MHz, δ): 9.30 (s, 1H, H-9), 8.86 (s, 1H, H-4), 8.24 (d, 2H, $^{3}J = 8.0$, H-13), 8.18 (s, 2H, H-19), 7.99 (d, 1H, $^{3}J = 7.5$, H-5), 7.76 (m, 3H, H-7, H-12), 7.60 (d, 1H, $^{3}J = 8.3$, H-8), 7.51 (t, 1H, $^{3}J = 7.5$, H-6), 7.14 (m, 2H, H-18), 6.73 (m, 2H, H-17). ^{13}C NMR (75.4 MHz, δ): 156.3 (C-2), 153.0 (C-8a), 146.8 (C-10), 146.1 (C-11), 145.2 (C-19), 135.8 (C-7), 134.4 (C-16), 133.5 (C-14), 133.1 (C-15), 133.0 (C-18), 132.2 (C-4), 131.1 (C-13), 130.0 (C-5), 126.1 (C-12), 125.8 (C-9), 123.6 (C-3), 123.5 (C-6), 119.8 (C-17), 118.6 (C-8), 116.8 (C-4a). ^{11}B NMR (128.3 MHz, δ): 0.25 (t, $J_{B\text{-}F} = 28$). ^{19}F NMR (376.3 MHz, δ in ppm): 144.64 (q, $J_{B\text{-}F} = 28$. FT-IR (cm^{-1}): 3039, 2037, 1718, 1611, 1274, 1039, 932, 895, 760, 547. HR-MS (ESI-TOF) *m/z* calcd. for $C_{26}H_{16}N_5O_2BF_2$ $[M+H]^+$: 480.1437, found 480.1437.

meso-(4-(1-((6-methoxy)2-oxo-2*H*-chromen-3-yl)-1*H*-1,2,3-triazol-4-yl))phenyl-4,4-difluoro-4-bora-3*a*,4*a*-diaza-*s*-indacene (**2b**).

Orange crystalline solid (54 %). Mp: 271–273 °C. ^{1}H NMR (400 MHz, $CDCl_3$, δ in ppm): 9.09 (s, 1H, H-9), 8.68 (s, 1H, H-4), 8.11 (d, 2H, $^{3}J = 8.2$, H-13), 7.96 (s, 2H, H-19), 7.69 (d, 2H, $^{3}J = 8.2$, H-12), 7.41 (d, 1H, $^{3}J = 9.1$, H-8), 7.24 (dd, 1H, $^{3}J = 9.1$, $^{4}J = 2.9$, H-7), 7.12 (d, 1H, $^{4}J = 2.9$, H-5), 7.01 (m, 2H, H-18), 6.57 (m, 2H, H-17), 3.91 (s, 3H, CH_3). ^{13}C NMR (100.6 MHz, $CDCl_3$, δ): 157.0 (C-6), 155.9 (C-2), 147.2 (C-8a), 146.9 (C-10), 146.7 (C-11), 144.2 (C-19), 134.9 (C-16), 133.8 (C-15), 132.9 (C-4), 132.6 (C-14), 131.5 (C-18), 131.3 (C-13), 125.9 (C-12), 123.2 (C-3), 121.3 (C-9), 121.1 (C-7), 118.7 (C-17), 118.5 (C-4a), 117.9 (C-8), 110.4 (C-5), 55.9 (CH_3). ^{11}B NMR (128.3 MHz, $CDCl_3$, δ): 0.30 (t, $J_{B\text{-}F} = 29$). ^{19}F NMR (376.3 MHz, $CDCl_3$, δ): 145.08 (q, $J_{B\text{-}F} = 29$). FT-IR (cm^{-1}): 3182, 1724, 1570, 1269, 1134, 795, 700, 657. HR-MS (ESI-TOF) *m/z* calcd. for $C_{27}H_{18}N_5O_3BF_2$ $[M+H]^+$: 510.1544, found 510.1548.

meso-(4-(1-((7-diethylamino)2-oxo-2*H*-chromen-3-yl)-1*H*-1,2,3-triazol-4-yl))phenyl-4,4-difluoro-4-bora-3*a*,4*a*-diaza-*s*-indacene (**2c**).

Red solid (63 %). Mp: 236–237 °C. ^{1}H NMR (400 MHz, $CDCl_3$, δ): 8.97 (s,1H, H-9), 8.51 (s,1H, H-4), 8.09 (d, 2H, $^{3}J = 8.5$, H-13), 7.95 (s, 2H, H-19), 7.67 (d, 2H, $^{3}J = 8.5$, H-12), 7.45 (d, 1H, $^{3}J = 9.0$, H-5), 7.01 (d, 2H, $^{3}J = 4.0$, H-18), 6.70 (dd, 1H, $^{3}J = 9.0$, $^{4}J = 2.5$ Hz, H-6), 6.57 (m, 3H, H-8, H-17), 3.47 (q, 4H, $^{3}J = 7.0$, CH_2), 1.26 (t, 6H, $^{3}J = 7.0$, CH_3). ^{13}C NMR (100.6 MHz, $CDCl_3$, δ): 156.9 (C-2), 155.9 (C-7), 151.6 (C-8a), 146.9 (C-10), 146.4 (C-11), 144.1 (C-19), 134.9 (C-16), 134.6 (C-4), 133.5 (C-15), 133.2 (C-14), 131.5 (C-18), 131.2 (C-13), 130.1 (C-5), 125.8 (C-12), 121.1 (C-9), 118.6 (C-17), 116.8 (C-3), 110.3 (C-6), 107.2 (C-4a), 97.2 (C-8), 45.1 (CH_2), 12.4 (CH_3). ^{11}B NMR (128.3 MHz, $CDCl_3$, δ): 0.30 (t, $J_{B\text{-}F} = 29$). ^{19}F NMR (376.3 MHz, $CDCl_3$, δ): 145.51 (q, $J_{B\text{-}F} = 29$). FT-IR (cm^{-1}): 3413, 2347, 1635, 1319, 1261, 1154, 1042, 984, 758, 644, 565. HR-MS (ESI-TOF) *m/z* calcd. for $C_{30}H_{25}N_6O_2BF_2$ $[M+H]^+$: 551.2173, found 551.2174.

meso-(4-(1-((6-bromo)2-oxo-2*H*-chromen-3-yl)-1*H*-1,2,3-triazol-4-yl))phenyl-4,4-difluoro-4-bora-3*a*,4*a*-diaza-*s*-indacene (**2d**).

Orange crystalline solid (54 %). Mp: 267–268 °C. ^{1}H NMR (750 MHz, δ): 9.28 (s, 1H, H-9), 8.77 (s, 1H, H-4), 8.22 (m, 3H, H-5, H-13), 8.15 (s, 2H, H-19), 7.89 (dd, 1H, $^{3}J = 8.9$, $^{4}J = 2.3$, H-7), 7.80 (d, 2H, $^{3}J = 8.1$, H-12), 7.55 (d, 1H, $^{3}J = 8.9$, H-8), 7.11 (d, 2H, $^{3}J = 3.9$, H-18), 6.71 (d, 2H, $^{3}J = 2.7$, H-17). ^{13}C NMR (188.6 MHz, δ):155.9 (C-2), 152.0 (C-8a), 146.8 (C-10), 146.3 (C-11), 145.3 (C-19), 135.8 (C-7), 134.5 (C-16), 134.0 (C-4), 133.3 (C-15), 132.9 (C-14), 132.2 (C-18), 132.0 (C-13), 131.9 (C-5), 126.2 (C-12), 124.5 (C-3), 123.5 (C-9), 120.7 (C-6), 119.9 (C-17), 119.1 (C-8), 117.4 (C-4a). ^{11}B NMR (96.2 MHz, δ): 0.13 (t, $J_{B\text{-}F} = 29$). ^{19}F NMR (282.2 MHz, δ): 141.39 (q, $J_{B\text{-}F} = 29$). FT-IR (cm^{-1}): 3031, 1735, 1537, 1391, 1385, 1256, 1110, 1070, 775, 745, 717. HR-MS (ESI-TOF) *m/z* calcd. for $C_{26}H_{15}BBrF_2N_5O_2$ $[M+Na]^+$: 582.0350, found 582.0351.

meso-(4-(1-((6-chloro)2-oxo-2*H*-chromen-3-yl)-1*H*-1,2,3-triazol-4-yl))phenyl-4,4-difluoro-4-bora-3*a*,4*a*-diaza-*s*-indacene (**2e**).

Orange crystalline solid (63 %). Mp: >300 °C. ^{1}H NMR (750 MHz, δ): 9.29 (s, 1H, H-9), 8.79 (s, 1H, H-4), 8.22 (d, 2H, $^{3}J = 8.2$, H-13), 8.16 (s, 2H, H-19), 8.10 (d, 1H, $^{4}J = 2.4$, H-5), 7.80 (d, 2H, $^{3}J = 8.2$, H-12), 7.79 (dd, 1H, $^{3}J = 8.8$, $^{4}J = 2.4$, H-7), 7.62 (d, 1H, $^{3}J = 8.8$, H-8), 7.12 (d, 2H, $^{3}J = 3.9$, H-18), 6.72 (d, 2H, $^{3}J = 2.6$, H-17). ^{13}C NMR (188.6 MHz, δ): 155.9 (C-2), 151.6 (C-8a), 146.9 (C-10), 146.3 (C-11), 145.3 (C-19), 134.6 (C-16), 134.1 (C-4), 133.3 (C-15), 132.9 (C-7), 132.3 (C-14), 132.2 (C-18), 132.0 (C-13), 129.6 (C-6), 128.9 (C-5), 126.2 (C-12), 124.6 (C-3), 123.5 (C-9), 120.2 (C-4a), 119.9 (C-17), 118.9 (C-8). ^{11}B NMR (96.2 MHz, δ): 0.15 (t, $J_{B\text{-}F} = 29$). ^{19}F NMR (282.2 MHz, δ): 143.79 (q, $J_{B\text{-}F} = 29$). FT-IR (cm^{-1}): 3061, 2166, 1714, 1536, 1386, 1261, 1114, 1078, 980, 813, 744. HR-MS

(ESI-TOF) *m/z* calcd. for $C_{26}H_{15}BClF_2N_5O_2$ $[M+Na]^+$: 536.0873, found 536.0896.

meso-(4-(1-((8-ethoxy)2-oxo-2*H*-chromen-3-yl)-1*H*-1,2,3-triazol-4-yl))phenyl-4,4-difluoro-4-bora-3*a*,4*a*-diaza-*s*-indacene (**2f**).

Red crystalline solid (67 %). Mp: 247–249 °C. ^{1}H NMR (750 MHz, δ): 9.26 (s, 1H, H-9), 8.80 (s, 1H, H-4), 8.22 (d, 2H, $^3J = 8.1$, H-13), 8.15 (s, 2H, H-19), 7.80 (d, 2H, $^3J = 8.1$, H-12), 7.50 (d, 1H, $^3J = 7.7$, H-7), 7.42 (d, 1H, $^3J = 7.7$, H-5), 7.40 (t, 1H, $^3J = 7.7$, H-6), 7.12 (d, 2H, $^3J = 3.9$, H-18), 6.71 (d, 2H, $^3J = 2.0$, H-17), 4.23 (q, 2H, $^3J = 6.9$, CH_2), 1.43 (t, 3H, $^3J = 6.9$, CH_3). ^{13}C NMR (188.6 MHz, δ):156.1 (C-2), 146.9 (C-11), 146.2(C-8, C-10), 145.3 (C-19), 142.4 (C-8a), 136.1 (C-4), 134.5 (C-16), 133.2 (C-15), 133.1 (C-14), 132.1 (C-18), 132.0 (C-13), 126.1 (C-12), 125.9 (C-6), 123.7 (C-3), 123.6 (C-9), 121.0 (C-7), 119.9 (C-17), 119.3 (C-4a), 116.6 (C-5), 65.1 (CH_2), 15.1 (CH_3). ^{11}B NMR (96.2 MHz, δ): 0.13 (t, $J_{B\text{-}F} = 29$). ^{19}F NMR (282.2 MHz, δ): 143.79 (q, $J_{B\text{-}F} = 29$). FT-IR (cm^{-1}): 2983, 1717, 1541, 1385, 1260, 1150, 1075, 977, 775. HR-MS (ESI-TOF) *m/z* calcd. for $C_{28}H_{20}BF_2N_5O_3$ $[M+H]^+$: 524.1700, found 524.1706.

meso-(4-(1-((7-hydroxy)2-oxo-2*H*-chromen-3-yl)-1*H*-1,2,3-triazol-4-yl))phenyl-4,4-difluoro-4-bora-3*a*,4*a*-diaza-*s*-indacene (**2g**).

Red crystalline solid (52 %). Mp: 239–241 °C. ^{1}H NMR (300 MHz, δ): 9.21 (s, 1H, H-9), 8.70 (s, 1H, H-4), 8.20 (d, 2H,$^3J = 8.3$, H-12), 8.16 (s, 2H, H-19), 7.81 (d, 2H, $^3J = 8.3$, H-13), 7.78 (d, 1H, ^{3}J = 8.6, H-5), 7.13 (m, 2H, H-18), 6.93 (dd, 1H, $^3J = 8.6$, $^4J = 2.3$, H-6), 6.89 (d, 1H, $^4J = 2.3$, H-8), 6.72 (m, 2H, H-17). ^{13}C NMR (75.4 MHz, δ): 163.2 (C-7), 156.8 (C-2), 155.3 (C-8a), 146.9 (C-10), 145.9 (C-11), 145.2 (C-19), 137.4 (C-16), 134.5 (C-4), 133.2 (C-15), 133.1 (C-14), 132.2 (C-18), 131.9 (C-13), 131.5 (C-5), 125.9 (C-12), 123.7 (C-9), 119.8 (C-17), 119.5 (C-3), 114.9 (C-6), 110.7 (C-4a), 102.2 (C-8). ^{11}B NMR (96.2 MHz, δ): 0.28 (t, $J_{B\text{-}F} = 29$). ^{19}F NMR (282.2 MHz, δ): 145.48 (q, $J_{B\text{-}F} = 28$). FT-IR (cm^{-1}): 3286, 2964, 2145, 1723, 1599, 1354, 1258, 1119, 1077, 774. HR-MS (ESI-TOF) *m/z* calcd. for $C_{26}H_{16}BF_2N_5O_3$ $[M+H]^+$: 496.1387, found 496.1384.

2.2. Single crystal X-ray molecular structure

Single crystals of compound **2a**, suitable for X-ray diffraction, were obtained from a saturated solution of 1,2-dichlorobenzene (DCB) as the monosolvate (**2a•DCB**). Several efforts to obtain single crystals of **2b-g** were unsuccessful. The monocrystal data of **2a•DCB** were recorded on a Bruker D8 VENTURE diffractometer using a graphite monochromator (Cu K_α, $\lambda = 1.54184$) at 185(2) K. The SAINT [54] and SORTAV software [55] were used to carry out the cell refinement and data reduction, respectively. The structures were solved by direct methods using the SHELXS-97 program [56] of the WINGX package [57]. The full-matrix least-squares methods were used to perform the final refinement with the SHELX97 program [56]. The H atoms on C, N, and O were geometrically positioned and treated as riding atoms with: C–H = 0.93−0.98 Å, Uiso(H) = 1.2 eq(C) for aromatic carbon atoms. Figures for publication were prepared with Platon [58]and Mercury [59]. General crystallographic data for compound **2a**, has been deposited in the Cambridge Crystallographic Data Centre (CCDC) as supplementary publication number 1994818.

2.3. Hirshfeld surface (HS) analysis and energy-framework diagrams

These calculations were performed with the software CrystalExplorer17.5 [60]. The HS was mapped over d_{norm} [61]. The energy components E_{elect} (electrostatic potential), E_{disp} (dispersion), E_{pol} (polarization), and E_{total} (total energy) were calculated by CrystalExplorer17.5-Gaussian 09 software [62] tandem, using the B3LYP/6-31G (d,p) level of theory. Scale factors [60] and % contribution of individual components to the stabilization energy [63] were also calculated. The interaction energy calculations were performed with the CLP-PIXEL software [64].

2.4. UV–vis and emission spectra

The UV–vis and emission spectra were recorded with a PerkinElmer Lambda XLS spectrophotometer and PerkinElmer LS55 fluorescence spectrometer, respectively, using 1 cm path length cuvettes of quartz at room temperature. Thin films of BPhTCs **2a-2g** were supported on a quartz surface by self assembly [65] through immersion in THF solutions (4×10^{-4} M, 517 nm) during 40–50 min, for absorption and emission measurements. Fluorescence quantum yields (φ) were measured in THF solutions, using fluorescein in 0.1 M NaOH (φ = 0.92) as a standard, as follows:

$$\varphi_{sample} = \varphi_{std} * \frac{A_{std} * F_{(area)sample}}{A_{sample} * F_{(area)std}} * \left(\frac{\eta_{solvent\ sample}}{\eta_{solvent\ std}}\right)^2$$

Where A is absorbance, F is the area under emission spectrum, η is the refractive index and std the standard.

2.5. Thermal analysis

Q2000 equipment and a Thermobalance Q5000 IR, of TA instruments, were used to perform DSC and TG measurements, respectively. A quantity of approximately 3.0–5.0 mg of sample, a gradient of 5.0 °C/min, a temperature interval from room temperature to 350 °C, under air flux of 25 mL/min in an open (TG), or pin-holed panels (DSC) were used.

2.6. Powder X-ray diffraction

Room temperature X-ray powder diffraction data were collected on a PAN Analytical X'Pert PRO diffractometer with Cu Kα1 radiation (λ = 1.5405 Å, 45 kV, 40 mA) or on a D8 Focus Bruker AXS instrument using Cu Kα1 radiation (λ = 1.542 Å, 35 kV, 25 mA).

The estimation of the crystallite size was carried out by the Scherrer equation [66]. The amorphousness and crystallinity percentages were calculated from the global and reduced area.

2.7. Computational methods

Gaussian 09w [62] package was used to perform density functional theory (DFT) calculations with the BVP86 method, the 6-31G (d,p) basis set theory level, and the DEF2TZV fitting set. The frontier molecular orbital (FMO) energy levels were calculated in the optimized geometry. Linear transitions of absorption were estimated from the optimized molecular structures using time-dependent DFT (TDDFT) methods [67] at the ωB97X-D/DGDZVP level of theory with CPCM model [68] in THF. The first ten electronic transitions were obtained from the optimized structures.

2.8. Electrochemical characterization

Cyclic voltammetry (CV) was performed with a PARSTAT® 2273 potentiostat-galvanostat. An electrochemical 3-electrodes cell was used: a saturated calomel electrode (SCE), a platinum wire and a graphite coated with **2a-g** films as reference electrode, auxiliary electrode and working electrode, respectively. A solution of 0.1 M Bu_4NPF_6 in anhydrous acetonitrile was used as the electrolyte. The experiments were carried out at room temperature, with a prior injection of nitrogen to deoxidize the system, and at a scan rate of 50 mV/s. The films were deposited on the working electrode by self-assembly [65] on a graphite surface of 0.25 cm^2 using a saturated solution of the corresponding compound in THF as solvent. Ferrocene-ferrocenium (Fc/Fc^+) couple was the internal standard. The energy levels of the FMOs (EH^{EC} and EL^{EC}) and electrochemical band gap (Eg^{EC}) values were calculated from the oxidation and reduction potentials in the corresponding onsets ($E_{onset(Ox)}$ and $E_{onset(Red)}$), using the empirical equations: $EH^{EC} = -e(E_{onset(Ox)} + 4.4)$, $EL^{EC} = -e(E_{onset(Red)} + 4.4)$ and $Eg^{EC} = -(EH^{EC} - EL^{EC})$, as reported [69,70].

2.9. Film resistivity measurements

BPhTCs **2a-g** were deposited on glass slides from THF solutions as thin films. Thickness measurements were performed with AMBIOS XP-100 Thickness Profilometer (A = 1 cm^2, thickness = 580–620 nm). Signatone Pro-4 of Lucas Labs, configured with inline four point probe [71], was used for sheet resistivity measurements with squared probes, the contact points were distanced such as: S_{12}=$S_{23} = S_{34} = S = 1$ mm.

2.10. Manufacture and electric characterization of OFET devices

OFET devices were manufactured following a top-contact/bottom-gate architecture with Indium Tin Oxide (ITO) films of 1.0 × 0.5 inch and 100 nm film thickness (surface resistivity 60 Ω/sq) as flexible substrate. The ITO films were previously sonicated in a mixture of tridistilled water and isopropyl alcohol (1:1) during 10 min and then ozonized under UV light during 15 min. Using a 12 μm pulsed CO_2 laser, one ITO substrate underwent patterning of source-drain contacts resulting in a channel of 1.0 cm wide (W) and 60 μm length (L). Next, solutions of OSs **2a-g** in THF (2×10^{-4} M), were deposited by the Drop-Casting method [72] onto the channel and contacts, followed by the placement of a polydimethylsiloxane (PDMS) layer using the Doctor Blade technique [73]. The device was finally assembled with placing the ITO gate substrate. The electric characterization of compounds **2a-g**, was performed in a system of two Keithley Source Meter (SMU) models 2400c y 2450 equipment, including the following: on/off ratio (I_{ON}/I_{OFF}) and field effect mobility at saturation regime (μ_{FET}). The reported values are the mean of at least three devices per each OS. All measurements were conducted under ambient temperature and atmosphere. The electric circuit and the architecture of OFETs are depicted in Fig. S1.

From the output characteristics, the lineal and saturation regimes are distinguished. In this work, the mobility of charges was calculated under the saturation regime when $V_D > (V_G - V_T)$, in this case, the following equation is used to calculate the μ_{FET} from the transference plot:

$$\mu_{FET} = \left(\frac{2L}{WC}\right)\left(\left(\frac{\delta\sqrt{I_D}}{\delta V_G}\right)_{V_D}\right)^2$$

Where L and *W* are the length and width of the channel, respectively, and *C* is the capacitance of the insulator per unit area (5.3 μFcm^{-2}).

2.11. Characterization of BPhTCs films by AFM

AFM analysis was performed on films generated by spin coating, using 1 mg/mL solutions of each compound in chloroform. They were deposited at 3500 rpm for 1 min. The thicknesses were measured by AFM, ranging from 14 to 114 nm. Detailed values are listed in Table S7. The atomic force microscope (3D Bioscope Catalyst, Bruker, USA) coupled to an inverted optical microscope (Axio Observer Z1, Zeiss, Germany) was used to run the experiments. The samples were directly deposited on the microscope plate and scanned in ScanAsyst mode using RTESP-300 probes (k = 40 N/m, tip radius = 8 nm, f_0 = 300 kHz). The analyses were run under air at laboratory conditions (T = 20 °C). The average arithmetic roughness (R_a) was estimated in the height images with scan areas of 10 × 10 μm^2,

using the NanoScope v. 1.40 software (Bruker).

3. Results and discussion

3.1. Synthesis and characterization

A conventional two-steps one pot protocol for BODIPYs synthesis was followed. Benzaldehydes **1a-g** were reacted with pyrrole in the presence of TFA, as catalyst, to afford the corresponding dipyrromethanes, which were further oxidized *in situ* with DDQ, followed by a complexation step using BF_3–OEt_2 in the presence of Et_3N, leading to the formation of the corresponding BPhTCs **2a-g**, Scheme 1. After column chromatography, compounds **2a-g** were isolated in moderate yields, 52–67 %, which are in the reported range for other BODIPYs or even larger [74]. Evidence of the boron-fluorine coupling was obtained from all spectra in which a triple signal at δ 0.13 to 0.30 for ^{11}B-NMR ($J_{B\text{-}F} = 28$–29 Hz) and a quadruple signal (1:1:1:1) at −143.0 to −145.0 ppm for ^{19}F ($J_{F\text{-}B} = 29$ Hz) were observed, in agreement with other *meso*-aryl-BODIPYs [75].

3.2. Molecular and supramolecular structure of BPhTC 2a-DCB

The molecular structure of **2a** was confirmed by single crystal X-ray. The ORTEP plot is depicted in Fig. 2(a); compound **2a** crystallized in the triclinic system, space group *P-1* and Z = 2 with one molecule of 1,2-dichlorobenzene as crystallization solvent (**2a-DCB**). The crystal data collection and refinement parameters of **2a-DCB** are listed in Table S2 and selected geometric parameters in Table S3. Bond lengths and angles in the coumarin [76], triazole [45] and BODIPY [11,12] fragments are in the characteristic range for analogous molecules. Particularly the C19–C22 length (1.477(4) Å) is in the reported range for other *meso*-substituted BODIPYs [31]. The coumarin heterocycle is forming angles of 10.20(9)° with the triazole ring, 1.97(7)° with the phenyl ring and 55.50(5)° with the BODIPY ending, in agreement with other reported *meso*-aryl substituted BODIPYs (53–56°) [77]. Therefore, the molecule is almost planar in the 4-pheny-1,2,3-triazolyl-coumarin (PhTC) fragment, but the BODIPY ending is in synclinal disposition.

The crystal lattice is structured through the participation of C5–H5···N13 and C8–H8···O1 weak hydrogen bonding interactions to develop 1D tapes along the [−1 1 5] direction, Fig. 2(b). Both interactions describe ring motifs whose graph set descriptors are $R_2^2(16)$ and $R_2^2(8)$, respectively. Coumarin carbonyls self-assemble the TC moieties through C2O2···C2O2 interactions of antiparallel type [78], directing the stacking in 2D along the (1 1 1) family of planes. The stacking is complemented by parallel displaced π-π* stacking interactions, one of them between the triazole and the benzofused coumarin ring, Cg1···Cg4, as has been observed in coumarins [76, 79] and between two pyrrole rings, Cg3···Cg3. The third dimension is developed through several C–Y···A (Y═H, O; A = π, F) close contacts, Fig. 2(c). Among non-covalent interactions, the π−π stacking is considered as the most efficient for transporting charge carriers [80]. The geometric parameters related to non-covalent interactions are listed in Tables S4 and S5.

3.3. Hirshfeld surface and quantitative interaction energy analysis of 2a•DBC

The Hirshfeld surface (HS) of **2a·DCB**, mapped over the d_{norm} (range = −0.2612 a 1.3011 atomic units), is shown in Fig. 3(a). The red bright spots highlight the dominant interactions, which are given by X···Y (X = H, C; Y═N, O, F, Cl) interactions. Among all the close interactions, Y···H/H···Y (Y═N, O, F, Cl) are the largest contributors to the surface (34.8 %), followed by H···H contacts (25.3 %), C···H/H···C (23.7 %), and at last the sum of C···Y/Y···C (14.8 %, Y═C, N, O, F, Cl). The percent contributions to the HS are shown in Fig. 3(b).

Selected results of interaction energies are listed in Table 1. Those contacts with total interaction energy (E_{tot}) values larger than −20.0 kJ mol^{-1} were omitted from discussion. The first directing energy contributor to the framework of **2a** is the assembly of C21–H21···Cg2, C2–O2···Cg5 and Cg1···Cg4 dispersive interactions (%E_{dis} = 85.6 %) which sum an E_{tot} value of −64.5 kJ mol^{-1}. The second and third energy contributors are C5–H5···N13 (E_{tot} = −42.5 kJ mol^{-1}; %$E_{dis=}$43.8) and C2–O2···C2 (E_{tot} = 40.5 kJ mol^{-1}; %$E_{dis=}$74.4), respectively. Finally, the energies of C8–H8···O1, C30–H30···F34 and Cg3···Cg3 interactions contribute with E_{tot} in the −25.5 to −27.4 kJ mol^{-1} each. Then, the lattice of **2a•DCB** is mainly stabilized by dispersive energy coming from the already non-covalent interactions early described. The larger contribution of E_{dis} is best appreciated in the Energy-framework diagrams for E_{ele}

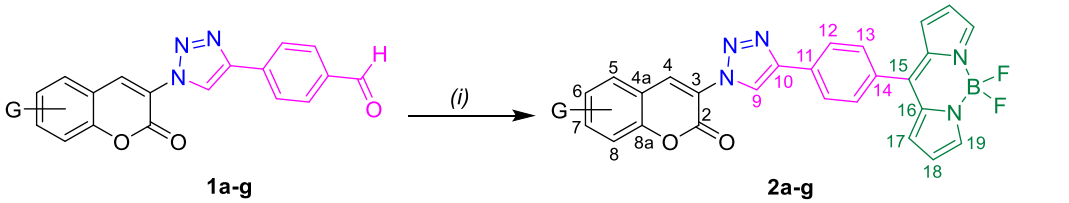

Scheme 1. Two-steps, one pot synthesis of BPhTCs. (*i*) Pyrrole, TFA, DDQ (1.2 eq.), Et_3N (10 eq.), BF_3-$(OEt)_2$ (15 eq.) in CH_2Cl_2. Yields of **2a-g** are in parenthesis.

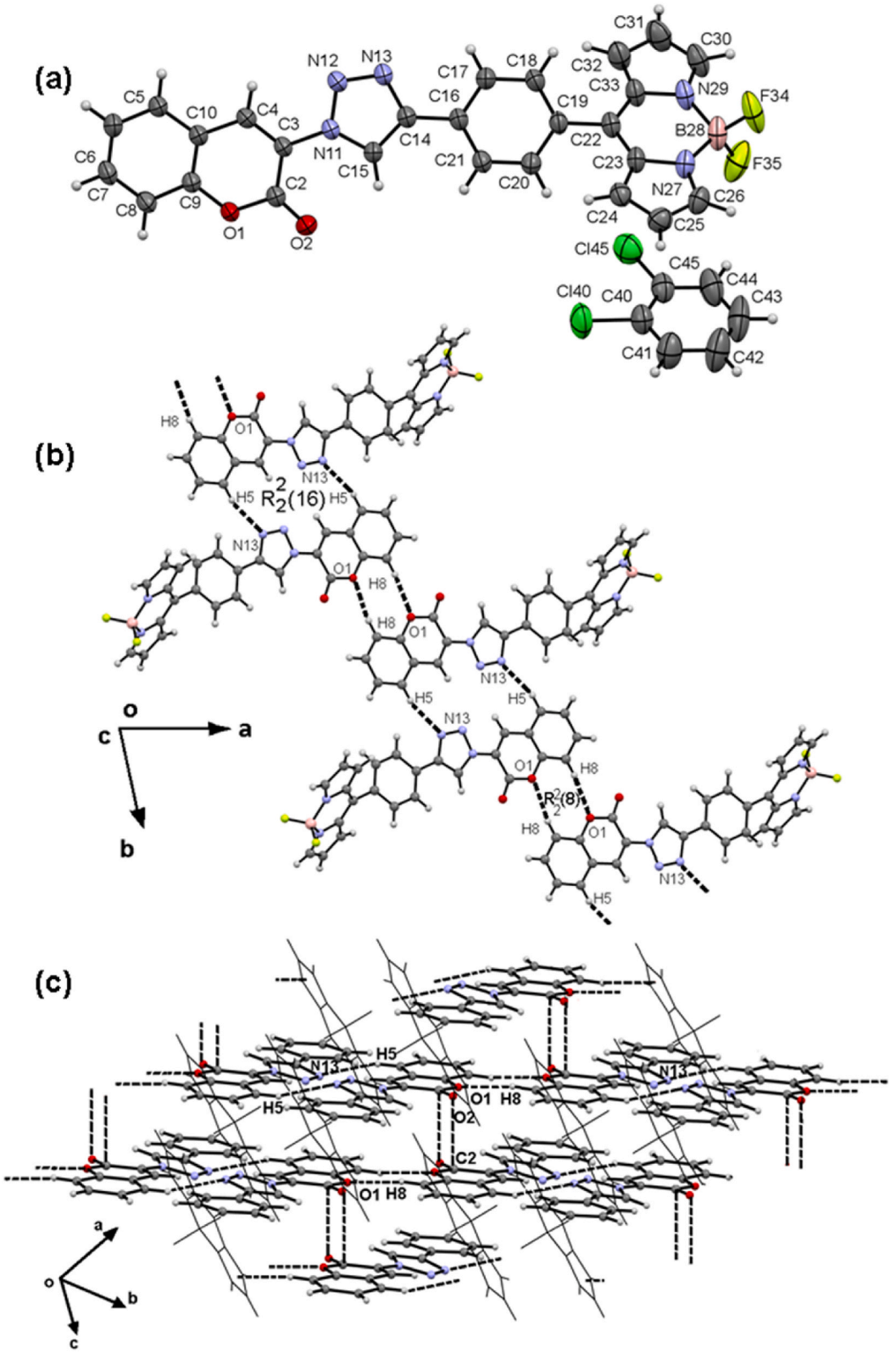

Fig. 2. (a) ORTEP plot of BPhTC **2a** at 50 % ellipsoid probability level with one molecule of 1,2-dichlorobenzene, used as crystallization solvent. (b) View in the *ab* plane, showing the supramolecular architecture developed by C–H··· A (A = N, O) interactions. (c) π-Stacking through carbonyl … carbonyl dipolar n→π* and parallel displaced π … π* interaction in the (1 1 1) family of planes, the BODIPY ending is drawn in solid lines.

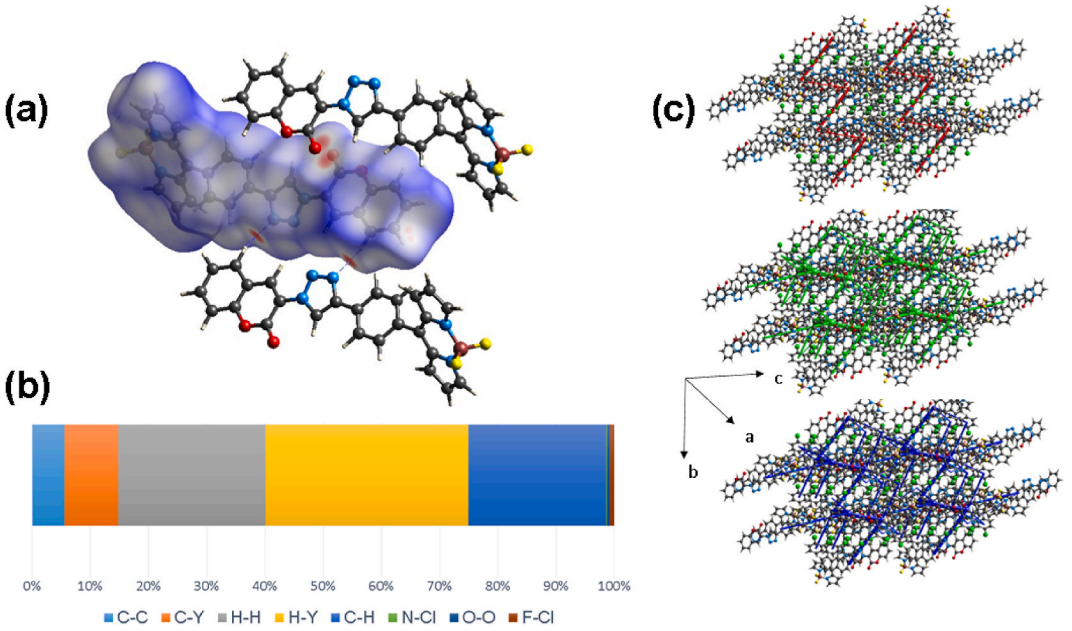

Fig. 3. (a) View of the Hirshfeld surface of BPhTC **2a**, mapped over d_{norm} −0.2612 to 1.3011 range in a.u. Hydrogen bonding is represented by dashed lines. (b) Comparative percent contributions in the Hirshfeld surface, (Y═N, O, F, Cl). (c) Energy-framework diagrams for E_{ele} (red), E_{dis} (green) and E_{tot} (blue) for a cluster of nearest-neighbor molecules in **2a**, cylinder scale of 80 for energy and cut-off = 10 kJ mol^{-1} in 2^3 unit cells. Note the large contribution of dispersive energy, in green, to the stabilization of the crystal network. DCB was omitted for clarity. (For interpretation of the references to colour in this figure legend, the reader is referred to the Web version of this article.)

Table 1
Calculated interaction energies (kJ mol^{-1}), $\%E_{comp}$ contributions to stabilization energy for selected HB and close contacts in BTC **2a**.

Interaction	$-E_{ele}$	$-E_{pol}$	$-E_{dis}$	E_{rep}	$-E_{tot}$	$\%E_{ele}$ [a]	$\%E_{dis}$ [a]	R [b]
C21–H21···Cg2^{iv,c}	9.5	5.5	89.5	44.8	64.5	9.1	85.6	7.11
C2–O2···Cg5^{iv,c}								
Cg1···Cg4^{viii,c}								
C5–H5···N13^{i}	35.8	9.3	35.1	52.9	42.5	44.6	43.8	11.9
C2–O2···C2^{vi}	12.6	3.5	46.7	25.9	40.5	20.1	74.4	11.0
C8–H8···O1^{ii}	8.9	2.7	30.4	20.0	25.5	21.2	72.4	16.5
C30–H30···F34^{iii}	23.9	4.2	18.7	29.4	26.5	51.1	40.0	16.9
Cg3···Cg3^{vii,c}	7.6	3.3	30.8	16.1	27.4	18.2	73.9	13.6
C25–H25···Cg4^{v,c}	5.3	0.9	32.3	18.2	23.1	13.8	83.9	7.67

[a] The % contribution of E_{comp} ($\%E_{comp}$) is calculated through (E_{comp}/E_{stab}) × 100 where $E_{stab} = E_{ele} + E_{pol} + E_{disp}$.
[b] R = distance between centroids of the interacting molecules in Å.
[c] Cg is the centroid of the n ring formed by the atoms indicated in parenthesis: Cg1 (N11–C15), Cg2 (N27–C26), Cg3 (N29–C33), Cg4 (C5–C10) and Cg5 (C16–C21).

(red), E_{dis} (green) and E_{tot} (blue) for **2a**, shown in Fig. 3(c).

3.4. X-ray powder diffraction, thermal stability, and AFM morphological properties

The thermal stability was settled by thermogravimetry (TG) and differential scanning calorimetry (DSC). In both cases, the experiments were run under air. The thermograms of **2a-g** are displayed in Fig. 4. Compounds **2b**, **2c** and **2g** lose crystallization solvent before 150 °C, probably due to small amounts of surreptitious water and/or elution solvent remnants. However, BPhTCs **2a**, **2c-g** are thermally stable up to 250 °C, except for compound **2b** (6-OMe) which decomposed at 180 °C. Decomposition is a multistep process, with a clear melting point for **2b** and **2g**, and the lack of solid phase transitions as shown by DSC analyses. The complete TG, ΔTG and DSC graphs are depicted in Figs. S2–8.

The microcrystalline-amorphousness nature of BPhTCs was estimated by X-ray, the powder diffraction patterns of **2a-g** are depicted in Fig. 5. Broad lines characteristics of semicrystalline solids are observed in all diffractograms, allowing the estimation of **2a-g** crystallinity in the 35–50 % range. The lines broadness is mostly due to the presence of small particles of BPhTCs whose crystallite sizes are in the 22–35 nm range, except for **2b** of 61 nm. The estimated crystallinity and particle size values are included in Table S6. The XRPD pattern of **2a** is quite different than that obtained by monocrystal X-ray diffraction of **2a•DBC** (1,2-dichlorobenzene) solvate,

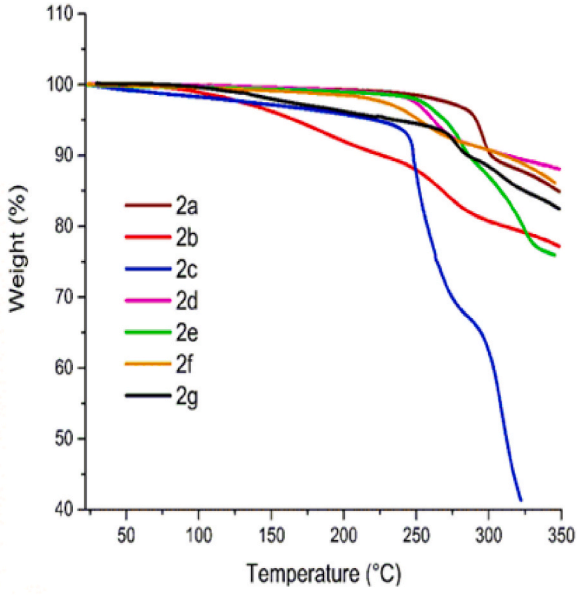

Fig. 4. Thermograms of BPhTCs **2a-g** recorded under air.

Fig. S9, in agreement the absence of DBC as crystallization solvent. Nevertheless, the molecular structures of **2a-g** are expected to be similar between them since all compounds possess the same basic structural unit.

Atomic force microscopy (AFM) measurements were performed to confirm the uniformity and morphology of the films formed by compounds **2a-g**. The average arithmetic roughness (R_a) was estimated in the height images with squared scan areas of 10^2 μm^2. All compounds formed continuous films on glass surface after spin-coating, the films are characterized for roughness (R_a) values in the 2.8–18 nm range, being that formed by compound **2a** the smoothest ($R_a = 2.8 \pm 0.5$ nm), a complete list of R_a values is in Table S7 and AFM images in Fig. 6. However, some films show plateau-type (**2c**, **2e**) or granulated (**2f-g**) aggregation domains within the continuous films, which could exert a fundamental role in determining the mobility of charges in thin film transistors [81].

3.5. *Photophysical properties*

The optical properties of **2a-g** were investigated by absorption-emission spectroscopy. Measurements were performed both in solution and in solid thin films. The corresponding data are summarized in Tables 2–3. The UV–vis absorption profiles of BPhTCs in THF solutions are shown in Fig. 7(a). Compounds **2a**, **2b, 2d,** and **2f** exhibit similar absorption profiles in solution, they show one absorption maximum (λ_1) centered at around 365–377 nm, attributed to the π–π* excitation from the PhTC moieties, and bathochromic shifted by 15–50 nm in relation to the parent PhTCs [51]. In contrast, the absorption profiles (λ_1) at high energy of BPhTCs **2c**, **2e** and **2g** show two absorption maxima approximately at ~361 and 418 nm each. In the region of longer wavelengths, BPhTCs show the absorption maxima (λ_2) at 500–502 nm, associated to the π–π* transition from the BODIPY unit [3,21].

The ε_2 values are within the same order of magnitude (~10^4 M^{-1} cm^{-1}), reaching the largest value in compound **2d** (10.6×10^4 M^{-1} cm^{-1}), effect attributed to the contribution of additional electronic density from the bromine lone pairs of electrons. As far as fluorescence quantum yield is concerned, the values are in the 0.004–0.0117 range, very similar to the value reported for *meso*-aryl-BODIPY ($\varphi = 0.065$) [80]. The normalized emission spectra of **2a-g** in THF, compared to fluorescein as a standard, as well as φ values are shown in Fig. S10. It is worth noting that the absorptions of the BODIPY unit in **2a-g** are very similar to the reported value for the absorption of *meso*-aryl-BODIPY ($\lambda_{abs} = 497$ nm) [82]. These results are explained because of the absence of conjugation between the PhTC and the BODIPY unit, and the small effect exerted by weak electron acceptor or donor groups in the BODIPY *meso*-aryl substituent [82].

Furthermore, in thin films, the absorption profiles of **2a-g** are quite different from solution, Fig. 7(c). They appear as two broad bands, the high energy band, associated to the coumarin transitions, exhibit hyperchromism whereas the BODIPY absorption hypochromism, compared to the solution spectra. This result indicates that the close packing of the molecular backbone within the thin films of BPhTCs improves the charge transfer into the coumarin. In general, the optical band-gap energies of **2a-g** (E_g^{opt}), obtained from the absorption spectra in thin films (2.20 ± 0.02 eV), are smaller by 6–8% than the values in solution (2.35 ± 0.01 eV) and independent from the substitution pattern and nature of the substituent in the coumarin unit.

The emission profiles of BPhTCs in THF solutions are shown in Fig. 7(b), and in their solid films thereof in Fig. 7(d). The data indicate that all compounds exhibit fluorescence in solution at λ_{em} in the 520–522 nm range, Table 2. This value is independent from the substitution pattern in the coumarin unit and very similar to the reported value for *meso*-aryl-BODIPY ($\lambda_{em} = 518$ nm) [82]. The coumarin emission band was totally suppressed and only the emission from the BODIPY ending was observed. Furthermore, the

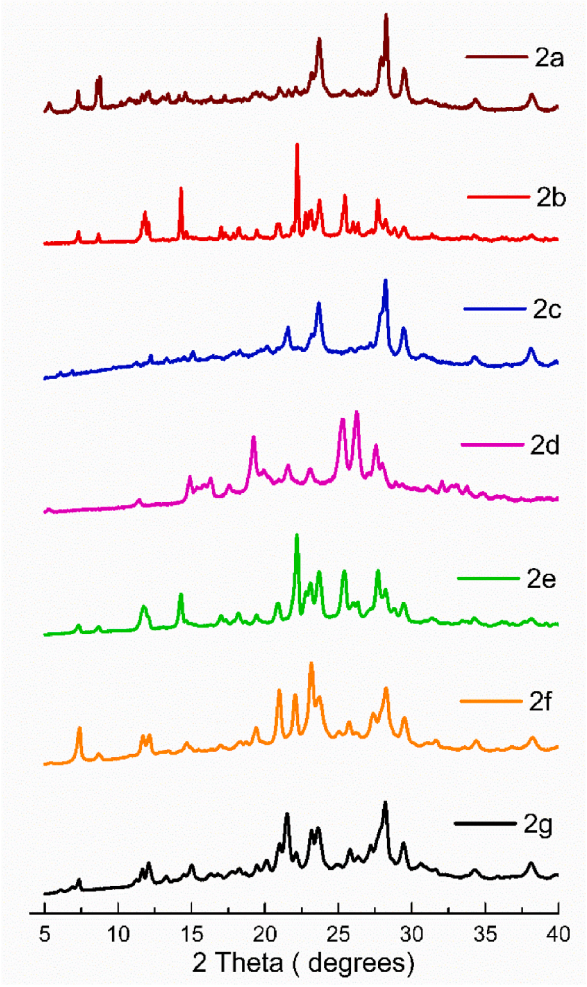

Fig. 5. X-ray powder diffractograms of **2a-g**.

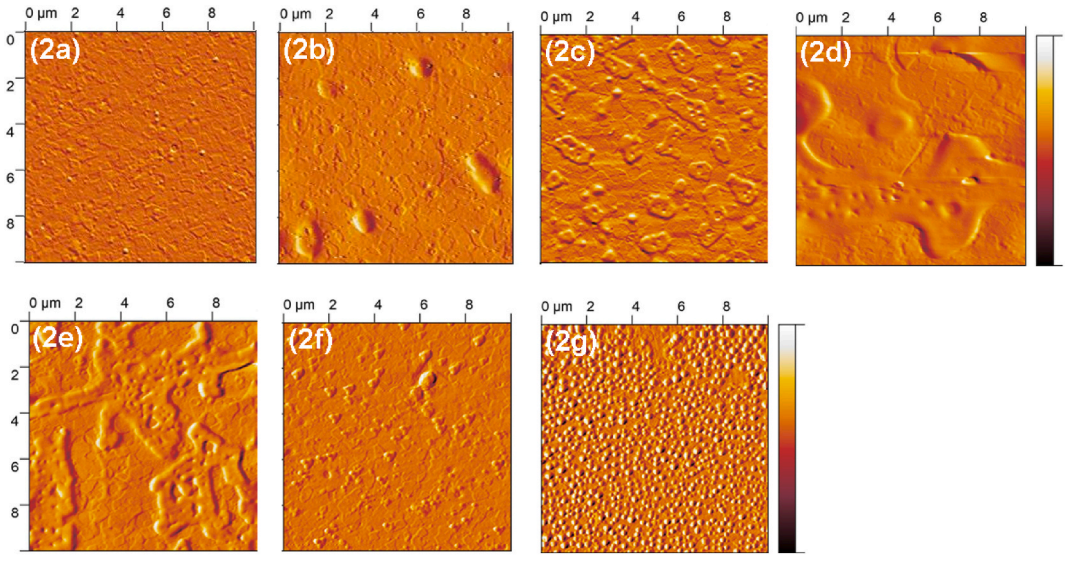

Fig. 6. AFM images of spin coated **2a-g** films (10 × 10 µm).

Table 2
Optical data of **2a-g** in THF solutions at room temperature.

BPhTC	λ_{abs}[a]/nm		$\varepsilon_2/10^4$ M^{-1} cm^{-1} (% error)	E_g^{opt}/eV	λ_{em}[b] /nm	Stokes shift/cm^{-1}	Fluorescence[c]
	λ_1	λ_2					
2a	365	500	4.78 (2.3)	2.35	520	769	5826
2b	377	501	4.87 (2.9)	2.36	521	766	7686
2c	363, 417	501	3.24 (0.9)	2.34	522	803	3269
2d	366	501	10.6 (0.8)	2.36	520	729	5514
2e	364, 417[d]	501	4.34 (1.0)	2.36	521	766	6392
2f	377	501	4.24 (0.6)	2.36	521	766	4581
2g	359, 419	502	1.52 (2.0)	2.36	520	690	4606

[a] Absorption in THF 2.5 X 10^{-5} M.
[b] Emission maximum in THF at 10^{-6} M, excited at the absorption maximum (λ_2).
[c] Measured from experimental emission spectra as the area under the curve in area units.
[d] Shoulder.

Table 3
Optical data of **2a-g** in solid films at room temperature.

BPhTC	λ_{abs}[a]/nm		E_g^{opt}/eV	λ_{em}[b]/nm	Stokes shift/cm^{-1}	Fluorescence[c]
	λ_1	λ_2				
2a	367	526	2.18	607	2537	1456
2b	381	522	2.22	606	2655	3538
2c	365	523	2.19	592	2229	1111
2d	379	522	2.20	604	2601	3702
2e	364	521	2.19	575	1806	1742
2f	375	527	2.19	562	1182	870
2g	372	518	2.22	584	2182	1954

[a] Absorption of thin solid films.
[b] Emission of thin solid film exited at the absorption maximum (λ_2).
[c] Measured from experimental emission spectra as area under the curve in area units.

emission maxima are red shifted in solid films as compared to THF-solutions by 84–87 nm (**2a-b** and **2d**), 64–70 nm (**2c** and **2g**) and 41–54 nm (**2e-f**), to reach the longest wavelength at 607 nm in compound **2a** and the shortest at 562 nm in compound **2f**, Table 3. The resulting fluorescence spectra are wide and almost symmetrical, the collection of which covers a larger part of the visible electromagnetic spectrum from green to red. In addition, the Stokes shift values in the solid, fold a minimum value of 1.8 (**2f**) to a maximum of 3.6 (**2d**) times the values in solution, indicating that decaying to the lowest vibrational level S_1 is highly favored in the solid, thus part of the energy is non-radiatively dissipated.

The emissive behavior of BPhTCs, in the solid, agrees with Twisted Intramolecular Charge Transfer (TICT) process characteristic of *meso*-aryl-BODIPYs [83]. The locally excited (LE) state of BPhTCs shapes a planar conformation in solution stabilized by electronic conjugation, which gives a sharp emission spectrum. In the solid, the intramolecular motion is restricted bringing the BPhTCs from the LE state to the TICT state, at which there is a total charge separation between BODIPY and the PhTC fragments. The TICT state has the effect of narrowing the band gap, red-shifting the emission spectrum but weakening the emission intensity through nonradiative quenching processes. The increased order in the solid, compared to solution, is given by the already described n→π* and pd π··· π* stacking interactions networking the crystal structure (*vide supra*).

3.6. Computational analysis

The calculated molecular structures, in the gas phase, of compounds **2a-g** predict an almost planar arrangement relying in the PhTC fragment. The calculated torsion angles between coumarin and triazole are in the 9.7–11.5° range, and between coumarin and phenyl are in the 0.1–1.5° range, but the BODIPY endings are 47.5–50.2° out of the mean coumarin plane, in good agreement with the torsion angles measured in the single crystal X-ray structure of **2a-DCB** (*vide supra*). Thus, the theoretical calculations are in good agreement with the geometry of the molecular structure observed by X-ray diffraction.

On the other hand, the challenge of acceptably predicting the electronic transitions of BODIPY derivatives has been reported in the literature [84,85]. The ωB97X-D model was chosen after comparing several commonly used models both in vacuum and with the CPCM model to estimate the electronic properties considering the contribution of the solvent [68,86]. The results of model comparisons can be found in the supplementary material S4. With all models, three main bands are predicted with a similar character of the transitions between the models, highlighting two more intense transitions. Acceptable approximations for BODIPYs derivatives have been reported with the ωB97X-D [84,87–89]. The most red-shifted electronic transition (around 430 nm) coincides with HOMO to LUMO (H→L) transition in six of the seven molecules studied, as expected. However, in the case of molecule **2c**, this band corresponds to a transition from HOMO-1 to LUMO (H-1→L). This behavior has been described both theoretically and experimentally, where the

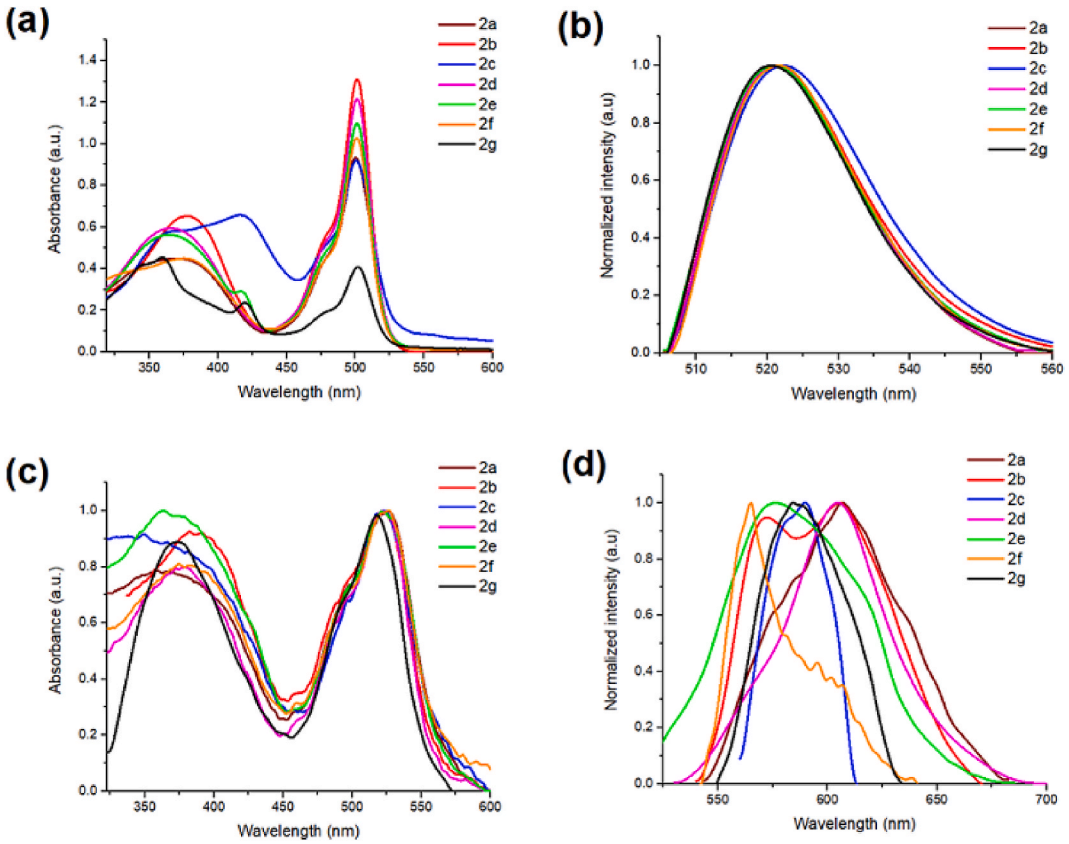

Fig. 7. Absorption and normalized emission spectra of BPhTCs **2a-g**. (a) Absorption and (b) emission in THF solutions at 10^{-6} M. (c) Absorption and (d) emission in thin films formed after three submersions of 15 min in THF solutions at 2×10^{-4} M.

lowest energy excited state level does not correspond to a HOMO/LUMO transition [90–92], including coumarin derivatives [93], such as **2c**. In this case, the diethylamino group, as an electron-donating group, modifies the energy of the HOMO [94,95] approaching the energy levels between HOMO and HOMO-1 (−4.94 eV and −4.91 eV, respectively. See Table S8) and enabling the HOMO-1 to LUMO transition [96].

The lowest energy transitions, their energies, oscillator strengths, and probable MO nature are summarized in Table 4. A complete list of the main transitions are tabulated in Table S8 and a pictorial representation of the lowest excited electronic transitions of BPhTCs are visualized in Fig. S11. The oscillator strength is a physical parameter that shows the allowedness in the radiative electronic transition of molecules and is directly proportional to the absorptivity coefficient [33]. Given the non-planar disposition between the BODIPY ending and the PhTC fragments, the *f* values of the H→L transition, around 0.53, are explained because of the weak mixing of the electronic wave functions.

The theoretical absorption spectra of the BODIPYs in THF solutions are shown in Fig. 8. The influence of the groups is reflected in the theoretical transitions, two main absorption regions, the first between 300 and 400 nm and the second between 400 and 500 nm are predicted. Molecules **2a**, **2b** (OMe), **2f** (OEt) and **2g** (OH) have similar theoretical spectra in terms of transitions and intensity, due to the influence of similar substituent groups. In addition, molecules **2d** (Cl) and **2e** (Br) differ only in the halide and show an almost identical spectrum. Finally, the spectrum of **2c** exhibited the highest intensity and the largest bathochromic shift of the high energy

Table 4
Computed lowest electronic transitions of BPhTCs **2a-2g** obtained by TDDFT ωB797X-D/DGDZVP, CPCM model in THF. Wavelength of absorption (λ_{abs}) in nm, energy (E) in eV, oscillation strength (OS, *f*), and MO character (% probability).

Compound	λ_{ab} / nm	E/eV	OS (*f*)	MO Character (%)
2a	431.11	2.8759	0.5524	H→L (96 %)
2b	431.61	2.8726	0.5478	H→L (96 %)
2c	431.49	2.8734	0.5447	H-1→L (96 %)
2d	431.73	2.8718	0.5492	H→L (96 %)
2e	431.75	2.8717	0.5490	H→L (96 %)
2f	431.69	2.8721	0.5471	H→L (96 %)
2g	431.53	2.8731	0.5479	H→L (96 %)

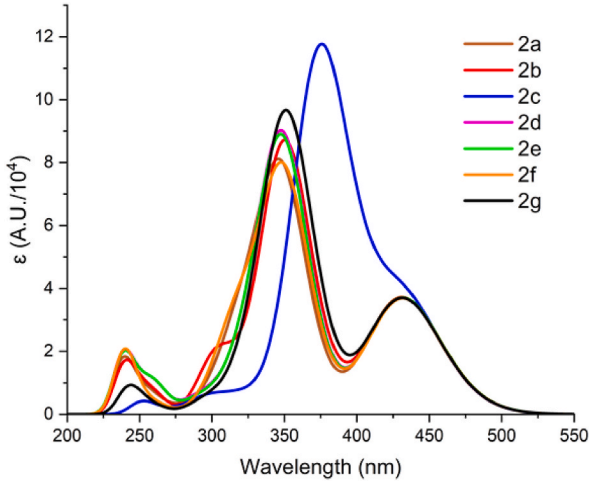

Fig. 8. Theoretical absorption spectra of **2a-2g**, obtained by TDDFT ωB797X-D/DGDZVP CPCM model in THF.

band. The most red-shifted transition of BPhTCs is theoretically predicted at a wavelength around 431 nm in all compounds, regardless the coumarin substituent, 93-84 nm at smaller wavelength than the experimental spectra, as has been reported for calculated spectra of aryl *meso*-aryl-BODIPYs [97].

The pictorial representations of the HOMO, LUMO, HOMO-1 and LUMO+1 FMOs of compounds **2a**, **2c**, and **2d**, as representative examples, are shown in Fig. 9. In general, the calculated absorption spectra of BPhTCs are consistent with what is observed in the experimental spectra. Then, the most red-shifted band, attributed to π→π* transition at 431 nm, defines the bandgap value of this family of compounds. The HOMO is localized on the BODIPY ending in all compounds, in agreement with reported calculations in other *meso*-aryl-BODIPYs [97,98]. On the other hand, the LUMO is centered in the whole molecule (**2a,b** and **2f,g**), on the TC fragment (**2d,e**), or on the BODIPY ending (**2c**), depending on the coumarin substituent. As mentioned before, the H-1→L transition is predicted to define the main transition in **2c**, H-1 is localized in the PhTC moiety. The effect of placing a BODIPY at one end of the PhTCs

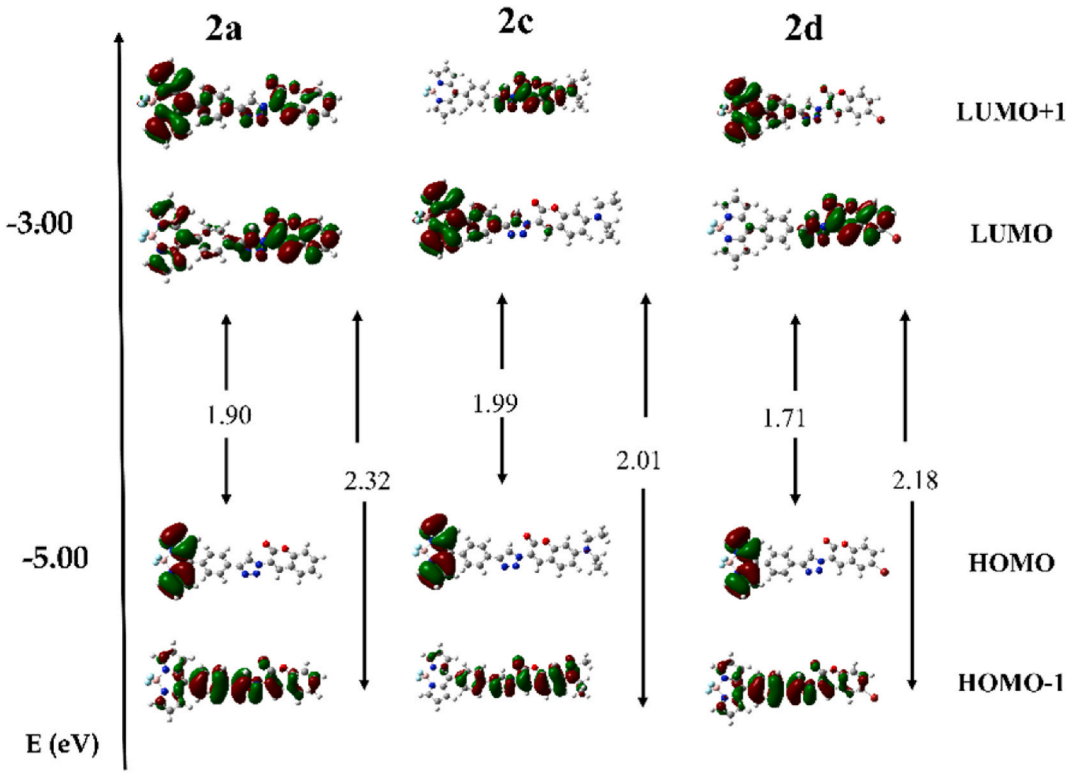

Fig. 9. Pictorial representation of HOMO, LUMO, HOMO-1, LUMO+1, energy distributions for **2a**, **2c**, and **2d**, involved in the absorption processes.

precursors (**1a-g**) [43] upshifts the energy of HOMO and downshifts the energy of the LUMO, to give bandgap values ($E^{DFT}_{H\rightarrow L}$) around 1.9 eV.

According to theoretical calculations, only the 7-NEt_2 group in the coumarin is capable to transform the TC moiety into the donor, making isoenergetic the HOMO-1 and HOMO FMOs, thus reverting the D-A nature of the BODIPY and coumarin fragments in **2c**.

In terms of resonance structures and donor-acceptor (D-A) properties of BPhTCs, that give rise to the experimental optical bandgaps ($E^{opt}_{H\rightarrow L}$), it can be accounted that the PhT fragment behaves as the donor and both the coumarin and BODIPY fluorophores behave as the acceptors, depending upon the substituent in the coumarin moiety. The proposed resonance structures **A** and **B** are depicted in Fig. 10. In BPhTCs bearing EW or ED groups on the 6- or 8- positions, the coumarin fragment exerts the role of the acceptor to develop the resonance form **A**. This behavior is reversed by 7-NEt_2 and 7-OH ED groups, forming the resonance structure **B**.

Besides, it is worth mentioning that the computed dipole moment (μ) is the largest for **2c** (15.8 D) and the shortest are for the halogenated compounds **2d** (8.2 D) and **2e** (8.1 D) whereas the rest of compounds show intermediate values. These results agree with the above proposal. In general, the charge separation is more effective upon the incorporation of the BODIPY ending to the PhTC fragment. A complete list of μ values can be found in Table 5.

3.7. Electrochemical characterization

Cyclic voltammetry (CV) allowed the evaluation of the electrochemical (EC) properties of **2a-g** in solid films. EC data are summarized in Table 5 and cyclic voltammograms of BPhTCs are shown in Figs. S12–18. The redox behavior of BPhTCs is characterized by a quasi-reversible process. The formation of π-radical anion is observed in the reduction zone with $E_{onset(Red)}$ values ranging between −0.42 and −0.74 V, attributed to the BODIPY unit, since it is easier to reduce than the coumarin fragment; these values are in the observed range for *meso*-aryl-BODIPYs [99]. In the oxidation region the formation of π-radical cation, attributed to the triazole donor, is observed. The $E_{onset(Ox)}$ values are in the 1.30–1.67 V range, values in the range reported for the starting PhTCs [51]. The EC energy of the HOMO (E^{EC}_{H}) and LUMO (E^{EC}_{L}) MOs, were obtained from the oxidation and reduction potentials in the onset, respectively [100]. The EC H→L gap ($E^{EC}_{H\rightarrow L}$) mean value is of 2.09 ± 0.08 eV for **2a-g**. The BODIPY moiety largely increases the electron-accepting capability of BPhTCs in comparison to their PhTCs precursors, with more impact in the LUMO than in HOMO energy levels.

Thus, the BODIPY attachment to the PhTC backbone has the effect of lowering the LUMO energy level, allowing the mobility of charges in compounds **2a-g**, as noted from optical and EC measurements, and theoretical calculations. In addition, the broad absorption spectrum in solid films, large extinction coefficients and Stokes shifts, could make BPhTCs potentially useful as electron transporting materials.

3.8. OFET electric characterization

To further study the electrical properties of compounds **2a-g**, organic field-effect transistors (OFET) were manufactured. As part of a first electrical characterization, films of BPhTCs were deposited on glass slides to measure their electrical resistivity. All compounds showed resistivity values between 10^4 and 10^5 Ωcm, listed in Table S9, typical values for semiconducting organic materials [21]. The semiconducting properties of BPhTCs, were measured at room temperature and atmosphere, using a top contact/bottom gate TFT device architecture in which an indium tin oxide (ITO) film on a flexible PET was used as the substrate for the source, drain and gate contacts, and polydimethylsiloxane (PDMS) as the dielectric film.

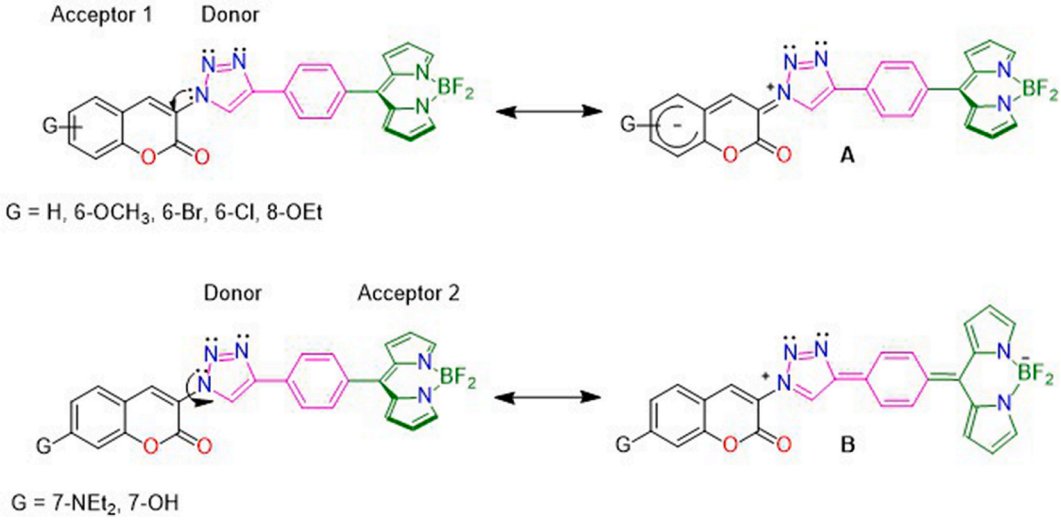

Fig. 10. Proposed resonance structures **A** and **B** for BPhTCs **2a-d**. **2a** (H), **2b** (6-OMe), **2c** (7-NEt_2), **2d** (6-Br), **2e** (6-Cl), **2f** (8-OEt) and **2g** (7-OH), the Coumarin and BODIPY endings act as the acceptors and the Ph-Triazole as the donor.

Table 5
EC properties from CV data and theoretical dipole moment of **2a-2g**.

BTC	$E_{onset(Red)}$ (V)	$E_{onset(Ox)}$ (V)	E_L^{EC} (eV)	E_H^{EC} (eV)	$E_{H\rightarrow L}^{EC}$ (eV)	Dipole moment (D)
2a	−0.68	1.40	−3.72	−5.80	2.13	10.7
2b	−0.58	1.48	−3.82	−5.88	2.06	12.2
2c	−0.66	1.59	−3.74	−5.99	2.25	15.8
2d	−0.46	1.62	−3.94	−6.02	2.08	8.2
2e	−0.53	1.49	−3.87	−5.89	2.02	8.1
2f	−0.42	1.67	−3.98	−6.07	2.09	12.2
2g	−0.74	1.30	−3.66	−5.70	2.10	11.8

I–V transfer characteristic curves were obtained by maintaining the source-drain voltage at 15 V and varying the gate voltage from −15 to 15 V forward and backward. The transfer curves are presented on both a linear scale in Fig. S19 and on a logarithmic scale ($Log_{10}|I_{DS}|$) in Fig. S20. Compounds **2a-g** showed similar behavior between them although in different current scales, ranging from ***μ***A (**2e-g**) to a few hundred mA (**2a-d**). All compounds displayed ambipolar behavior with typical V-shaped ($Log_{10}|I_{DS}|$) transfer curves, where the p-type behavior, characteristic of coumarins and frequently observed in *meso*-substituted BODIPYs [21], is present in the I–V transfer curves of the **2a-g** compounds. p-Type OS are more frequently described whereas the advances in n-type or ambipolar conjugated materials are scarce. Therefore, the n-channel behavior in the BPhTC-TFT devices at room temperature conditions was analyzed with the aim of contributing to this field of knowledge.

The coherent correspondence between the saturation currents, reached in the output curves, and the currents measured in the transfer curves of **2a-g** devices, is observed in Fig. S21 for positive V_G values. The output curves are reliable between 4 and 10 V in the gate, other voltages were not tested due to the early degradation of the OS and insulating materials. The carrier mobilities (μ_{FET}) were calculated considering an n-type channel, from Fig. S22, where the I_{DS} and $(I_{DS})^{1/2}$ currents are plotted versus V_G. The standard saturation regime quadratic model $\mu_{FET} = (2L/WC)((\delta(I_D)^{1/2}/\delta V_G))V_D)^2$ was used. From these plots, the I_{ON}/I_{OFF} current ratio of the **2a-g**-TFT device was also estimated, ranging from 10^2 (**2a-d**) to 10^5 (**2e-g**). A higher order I_{ON}/I_{OFF} ratio is not expected because the devices were operated at relatively low V_G voltages in contrast to the V_G values of up to 100 V used in polymer OFET devices [22]. The electrical characteristics of **2a-g**-OFET devices are summarized in Table 6. Even when their complete electric characterization can be found in Figs. S19–22, the characteristic I–V transfer and output curves (drain current versus drain voltage) as well as the transfer I–V curves in logarithmic scale for $|I_{DS}|$ and linear scale for the $|I_{DS}|^{1/2}$ are shown in Fig. 11(a) and (b) and 11(c),(d), respectively, for **2d**- and **2f**-OFET devices as representative examples.

Regardless the chemical structure of the BPhTCs, the saturation regime is reached in the 6–9 V range. However, the mobility of the charge carriers seems to depend on the OS performance, compounds **2a-d** exhibit μ_{FET} values of nearly $\sim 10^{-2}$ cm^2 V^{-1} s^{-1}, two orders of magnitude larger than the values exhibited by **2e-g** (10^{-4} cm^2 V^{-1} s^{-1}). Following a similar analysis for electron charge carriers, the hole mobilities were also estimated. The values are approximately one to two orders of magnitude smaller (7.4×10^{-4} **2a**, 6.3×10^{-3} **2b**, 4.7×10^{-3} **2c**, 1.0×10^{-3} **2d**, 3.9×10^{-6} **2e**, 2.5×10^{-6} **2f**, and 6.5×10^{-6} **2g**) than the corresponding electron mobilities in Tables 6 and in agreement with the better performance of compounds **2a-g** as n-type OSs. These marked differences are attributed to the inherent properties of the **2a-g** solutions to form a uniform and continuous deposit in the channel, whose integrity was tested by confocal microscopy taking advantage of their fluorescent properties. A cross-section view of a TFT device manufactured with OS **2c** (in red) on PET-ITO substrate (in gray) is shown in Fig. 12(a–c). Compounds **2a-d** were successfully layered in the channel from their THF solutions forming homogeneous deposits of ~10 μm thick. In contrast, the deposits of OS **2e-g** were stratified, generating defects that diminished the performance of the TFT devices. All our efforts to manufacture homogeneous deposits of compounds **2e-g** using the Drop-Casting method were unsuccessful. It has been reported that the measured mobilities depend on the method used to place the OS [23]. In addition, the low mobility of **2e-g** can be caused by structural defects, low charge interaction on the insulating-semiconductor surface [101] or the molecular packing in the solid state. A brief comparison among **2a-d** OS, which were capable to form processable deposits, and the device performance, indicate that substituents in both 6- and 7-positions gave good μ_{FET} values. Nevertheless, soft ED substituents, 7-NEt_2 and 6-Br groups, showed the best values of I_{ON}/I_{OF} ratio. These results point to OSs **2c** and **2d** as the best materials among this group of compounds with the additional bonus that they can be monitored thanks to their fluorescent properties.

Furthermore, OFETs made with BPhTCs **2a-d**, showed negligible degradation after one month of storage in air under ambient conditions of light and humidity. Even though, the measured μ_{FET} values are in the range reported for BODIPYs-OFET devices [21], the charge carrier mobility values, herein measured for the **2a-d**-OFET devices, are larger than those reported for other triazoles (3.8×10^{-5} cm^2 V^{-1} s^{-1}) [102], thiophene-BODIPYs (5.3×10^{-4} cm^2 V^{-1} s^{-1}) [17], triphenylamine-BODIPY-triphenylamine triads (10^{-5}-10^{-7} cm^2 V^{-1} s^{-1}) [103], carbazole-BODIPY-carbazole triads (10^{-5} cm^2 V^{-1} s^{-1}) [104] but similar to BODIPY-quaterthiophene-BODIPY crystalline fibers (10^{-2} cm^2 V^{-1} s^{-1}) [23], dimeric isoindigo-aza-BODIPY (1.1×10^{-1} cm^2 V^{-1} s^{-1}) [105], naphthalene-imide-BODIPYs (0.10 cm^2 V^{-1} s^{-1}) [106], among others.

Recalling the high degree of crystallinity of these compounds, estimated by XRPD measurements, the efficient charge transport and thus the performance of **2a-g** crystals depend not only on the molecular structure but also on non-covalent intermolecular interactions. Therefore, the mobility properties observed for **2a-d** can be attributed to their crystalline nature, whose crystal packing is ruled by C–H···A (A = N, O) interactions, π-stacking through carbonyl ···carbonyl dipolar n→π*, and parallel displaced π ··· π* interactions [77], as observed in the crystal network of the **2a** (*vide supra*).

Table 6
Semiconductor characteristics of compounds **2a-g**, measured under ambient temperature and atmosphere, in top-contact/bottom-gate TFT device architecture.

BPhTC	$\mu_{FET}/(cm^2\ V^{-1}\ s^{-1})$	I_{ON}/I_{OF}
2a	1.6×10^{-2}	2.1×10^{3}
2b	5.0×10^{-2}	4.6×10^{2}
2c	1.0×10^{-2}	3.1×10^{4}
2d	2.2×10^{-2}	2.4×10^{5}
2e	3.2×10^{-4}	4.0×10^{4}
2f	0.77×10^{-4}	4.3×10^{5}
2g	2.9×10^{-4}	3.3×10^{3}

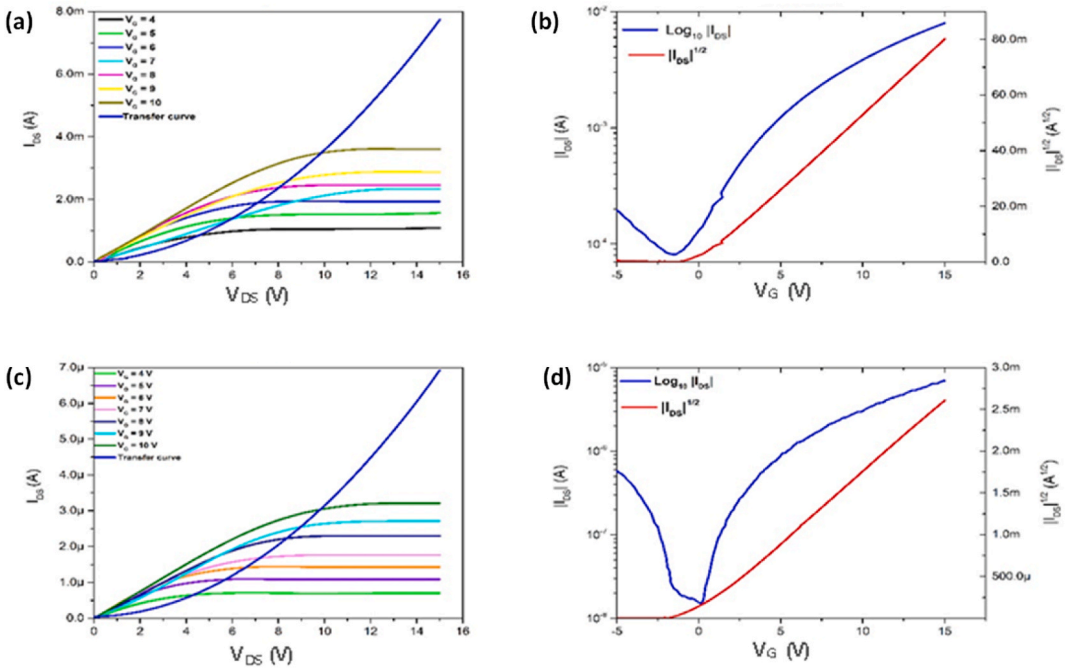

Fig. 11. Characteristic I–V transfer plots measured in the range of 4–10 V in the gate voltage (V_G) at ambient temperature and atmosphere, and I–V transfer plots in logarithmic scale of |IDS| and linear scale for the $|IDS|^{1/2}$, of **2d** (a), (b) and **2f** (c), (d) OFET devices.

4. Conclusions

Herein we report a comprehensive research of a series of structurally related BODIPY-1,2,3-triazolyl-phenyl-coumarin hybrid compounds (BPhTCs). Seven BODIPY labelled phenyl-triazole-coumarin derivatives **2a-g** have been synthesized, in moderate yields, using a simple methodology under mild conditions. The photophysical properties of BPhTCs depend on the nature of the coumarin substituent. Optical and electrochemical band-gap values in the solid are as small as ~2.20 and ~2.09 eV, respectively, ranking them as good prospects for semiconducting purposes which according with the substituent in the coumarin behave as A-D dyes being D the BODIPY or coumarin. Top gate/bottom-contact solution processed field-effect transistors of BPhTCs exhibit ambipolar behavior which exhibited *n*-channel charge carrier mobilities as high as 10^{-2} cm^2 V^{-1} s^{-1} and current on/off ratios of 10^2-10^5 under ambient conditions. It was also demonstrated, through single crystal X-ray analysis of **2a•DCB**, that the crystal network is developed through highly dispersive interactions: n-π* and π-π* stacking interactions, as well as C–H ⋯ A (A = N, O, π, F) close contacts, which rule the stabilization energy of the crystal and are responsible for transporting the charge carriers. Further efforts to obtain single crystals of this class of OSs for X-ray diffraction should be done to a better understanding of those supramolecular features that rule the performance of the OFET devices. Thus, the potential of BPhTCs as crystalline building blocks for small molecules organic semiconductor purposes with large Stokes shift, good thermal and air stability up to 250 °C, and good shelf life was demonstrated. The OSs **2c** and **2d** are the best materials among this group of compounds with the additional bonus that they can be monitored thanks to their fluorescent properties. The medium yields as well as the lack of processability of the most polar derivatives **2e-g** to form the OFET devices limit their high scale use. It is worth highlighting the use of THF both in optical studies and in the manufacturing of OFETs, which is considered an environmentally friendly solvent, out of the list of 'substances of very high concern' (SVHC). Finally, this work contributes on fundamental understanding between the relationship of the organic structures and charge transport properties. As a future

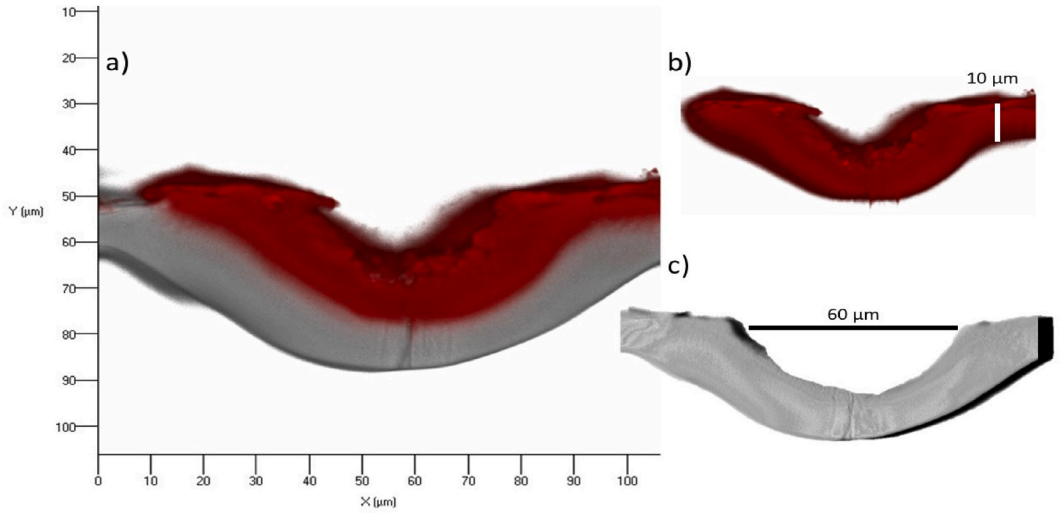

Fig. 12. (a) Confocal Microscopy of a cross-section of the OFET device manufactured with OS **2c** (in red) on PET-ITO substrate (in gray). Deposit thick (b) and channel wide (c) are shown. (For interpretation of the references to colour in this figure legend, the reader is referred to the Web version of this article.)

proposal, the synthesis of a polymer $(D\text{-}A)_n$ using the structures of **2a-*g*** as a repeating unit and including intermolecular spacers is suggested. For this purpose, the synthesis of new precursors enabling this polymerization must be considered, using environmentally friendly synthetic methods such as microwave and/or mechano-synthesis. The polymer could have better processability and film formation, which could improve OFET performance.

Data availability statement

Authors agree to make our data publicly available. Most of them are available in the Supplementary Material and crystallographic data was deposited as CCDC-1994818.

CRediT authorship contribution statement

José Emilio de la Cerda-Pedro: Writing - original draft, Methodology, Investigation. **Oscar Javier Hernández-Ortiz:** Methodology, Investigation, Formal analysis. **Rosa Angeles Vázquez-García:** Supervision, Methodology, Formal analysis. **Efrén V. García-Báez:** Methodology, Formal analysis. **Ramón Gómez-Aguilar:** Validation, Methodology, Investigation, Formal analysis. **Arián Espinosa-Roa:** Software, Methodology. **Norberto Farfán:** Supervision, Funding acquisition, Conceptualization. **Itzia I. Padilla-Martínez:** Writing - review & editing, Writing - original draft, Supervision, Resources, Project administration, Funding acquisition, Formal analysis, Conceptualization.

Declaration of competing interest

The authors declare the following financial interests/personal relationships which may be considered as potential competing interests: Itzia Irene Padilla-Martinez reports financial support was provided by National Council on Science and Technology (CONACYT now CONAHCYT, National Council on Humanities, Science and Technology), Mexico. Norberto Farfan reports financial support was provided by National Council on Science and Technology, Mexico. Jose Emilio de la Cerda-Pedro reports financial support was provided by National Council on Science and Technology, Mexico. Oscar Javier Hernandez-Ortiz reports financial support was provided by National Council on Science and Technology, Mexico. If there are other authors, they declare that they have no known competing financial interests or personal relationships that could have appeared to influence the work reported in this paper.

Acknowledgements

IIP-M gratefully acknowledges the financial support from CONACYT (grant 255354) and SIP-IPN. NF acknowledges the Faculty of Chemistry-UNAM (PAPIIT IN-200422 and PAIP 5000–9056) and CONACYT (A1-S7642). RG-A thanks to SIP-20200477. JEC-P and OJH-O thank CONACYT, for postdoctoral fellowships.

Appendix A. Supplementary data

Supplementary data to this article can be found online at https://doi.org/10.1016/j.heliyon.2023.e23517.

References

[1] O. Buyukcakir, O.A. Bozdemir, S. Kolemen, S. Erbas, E.U. Akkaya, Tetrastyryl-Bodipy dyes: convenient synthesis and characterization of elusive near IR fluorophores, Org. Lett. 11 (2009) 4644–4647, https://doi.org/10.1021/ol9019056.

[2] Y. Hayashi, N. Obata, M. Tamaru, S. Yamaguchi, Y. Matsuo, A. Saeki, S. Seki, Y. Kureishi, S. Saito, S. Yamaguchi, H. Shinokubo, Facile synthesis of biphenyl-fused BODIPY and its property, Org. Lett. 14 (2012) 866–869, https://doi.org/10.1021/ol2033916.

[3] A. Loudet, K. Burgess, BODIPY dyes and their derivatives: syntheses and spectroscopic properties, Chem. Rev. 107 (2007) 4891–4932, https://doi.org/10.1021/cr078381n.

[4] T.-y. Li, J. Benduhn, Y. Li, F. Jaiser, D. Spoltore, O. Zeika, Z. Ma, D. Neher, K. Vandewal, K. Leo, Small molecule near-infrared boron dipyrromethene donors for organic tandem solar cells, J. Mater. Chem. A. 6 (2018) 18583–18591, https://doi.org/10.1021/jacs.7b07887.

[5] A.M. Poe, A.M.D. Pelle, V. Subrahmanyam, W. White, G. Wantzb, S. Thayumanavan, Small molecule BODIPY dyes as non-fullerene acceptors in bulk heterojunction organic photovoltaics, Chem. Commun. 50 (2014) 2913–2915, https://doi.org/10.1039/C3CC49648A.

[6] D. Cortizo-Lacalle, C.T. Howells, U.K. Pandey, J. Cameron, N.J. Findlay, A.R. Inigo, T. Tuttle, P.J. Skabara, I.D.W. Samuel, Solution processable diketopyrrolopyrrole (DPP) cored small molecules with BODIPY end groups as novel donors for organic solar cells, Beilstein J. Org. Chem. 10 (2014) 2683–2695, https://doi.org/10.3762/bjoc.10.283.

[7] A. Senocak, E.N. Kaya, B. Kadem, T. Basova, E. Demirbas, A. Hassan, M. Durmus, Synthesis and organic solar cell performance of BODIPY and coumarin functionalized SWCNTs or graphene oxide nanomaterials, Dalton Trans. 47 (2018) 9617–9626, https://doi.org/10.1039/c8dt01588k.

[8] M. Poddar, V. Sharma, S.M. Mobin, R. Misra, 1,8-Naphthalimide-Substituted BODIPY dyads: synthesis, structure, properties, and live-cell imaging, Chem. Asian J. 13 (2018) 2881–2890, https://doi.org/10.1002/asia.201800816.

[9] D. Prasannan, C. Arunkumar, A "turn-on-and-off" pH sensitive BODIPY fluorescent probe for imaging E. coli cells, New J. Chem. 42 (2018) 3473–3482, https://doi.org/10.1039/C7NJ04313A.

[10] M. Chaari, N. Gaztelumendi, J. Cabrera-González, P. Peixoto-Moledo, C. Viñas, E. Xochitiotzi-Flores, N. Farfán, A.B. Salah, C. Nogu, R. Núñez, Fluorescent BODIPY-anionic boron cluster conjugates as potential agents for cell tracking, Bioconj. Chem. 29 (2018) 1763–1773, https://doi.org/10.1021/acs.bioconjchem.8b00204.

[11] R. Prieto-Montero, A. Prieto-Castañeda, R. Sola-Llano, A.R. Agarrabeitia, D. García-Fresnadillo, I. López-Arbeloa, A. Villanueva, M.J. Ortiz, S. de la Moya, V. Martínez-Martínez, Exploring BODIPY derivatives as singlet oxygen photosensitizers for PDT, Photochem. Photobiol. 96 (2020) 458–477, https://doi.org/10.1111/php.13232.

[12] A. Valdez-Calderón, M. Farfán-Paredes, X. Araujo-Padilla, M. Rodríguez, G. Ramos-Ortiz, N. Farfán, E. Ramón-Gallegos, Brominated BODIPYs as potential photosensitizers for photodynamic therapy using a low irradiance excitation, Polyhedron 176 (2020), 114207, https://doi.org/10.1016/j.poly.2019.114207.

[13] E. Xochitiotzi-Flores, A. Jiménez-Sánchez, H. García-Ortega, N. Sánchez-Puig, M. Romero-Ávila, R. Santillan, N. Farfán, Optical properties of two fluorene derived BODIPY molecular rotors as fluorescent ratiometric viscosity probes, New J. Chem. 40 (2016) 4500–4512, https://doi.org/10.1039/C5NJ03339J.

[14] E. Xochitiotzi-Flores, A.A. Islas-Mejia, H. García-Ortega, M. Romero-Ávila, J.M. Mendez-Stivalet, M.P. Carreón-Castro, R. Santillan, M. Maldonado-Domínguez, R. Arcos-Ramos, N. Farfán, On the structure of meso-substituted F-BODIPYs and their assembly in molecular crystals: an experimental-theoretical approach, J. Organomet. Chem. 805 (2016) 148–157, https://doi.org/10.1016/j.jorganchem.2016.01.021.

[15] M.M. Salim, E.A. Owens, T. Gao, J.H. Lee, H. Hyun, H.S. Choi, M. Henary, Hydroxylated near-infrared BODIPY fluorophores as intracellular pH sensors, Analyst 139 (2014) 4862–4973, https://doi.org/10.1039/C4AN01104J.

[16] C.L. Liu, Y. Chen, D.P. Shelar, C. Li, G. Cheng, W.F. Fu, Bodipy dyes bearing oligo(ethylene glycol) groups on the meso-phenyl ring: tuneable solid-state photoluminescence and highly efficient OLEDs, J. Mater. Chem. C 2 (2014) 5471–5478, https://doi.org/10.1039/C4TC00720D.

[17] M. Ozdemir, D. Choi, G. Kwon, Y. Zorlu, B. Cosut, H. Kim, A. Facchetti, C. Kim, H. Usta, Effect of AIE substituents on the fluorescence of tetraphenylethene-containing BODIPY derivatives, ACS Appl. Mater. Interfaces 8 (2016) 14077–14087, https://doi.org/10.1021/acsami.5b05033.

[18] J.J. Chen, S.M. Conron, P. Erwin, M. Dimitriou, K. McAlahney, M.E. Thompson, High-Efficiency BODIPY-based organic photovoltaics, ACS Appl. Mater. Interfaces 7 (2015) 662–669, https://doi.org/10.1021/am506874k.

[19] D. Ji, L. Jiang, H. Dong, Q. Meng, Y. Zhen, W. Hu, Silver mirror reaction for organic electronics: towards high-performance organic field-effect transistors and circuits, J. Mater. Chem. C 2 (2014) 4142–4146, https://doi.org/10.1039/C4TC00119B.

[20] T. Bura, N. Leclerc, S. Fall, P. Léveque, T. Heiser, P. Retailleau, S. Rihn, A. Mirloup, R. Ziessel, High-performance solution-processed solar cells and ambipolar behavior in organic field-effect transistors with thienyl-BODIPY scaffoldings, J. Am. Chem. Soc. 134 (2012) 17404–17407, https://doi.org/10.1021/ja3072513.

[21] D. Ho, R. Ozdemir, H. Kim, T. Earmme, H. Usta, C. Kim, BODIPY-based semiconducting materials for organic bulk heterojunction photovoltaics and thin-film transistors, ChemPlusChem 84 (2019) 18–37, https://doi.org/10.1002/cplu.201800543.

[22] H. Usta, M.D. Yilmaz, A.-J. Avestro, D. Boudinet, M. Denti, W. Zhao, J.F. Stoddart, A. Facchetti, BODIPY–Thiophene copolymers as p-channel semiconductors for organic thin-film transistors, Adv. Mater. 25 (2013) 4327–4334, https://doi.org/10.1002/adma.201300318.

[23] M. Ozdemir, D. Choi, G. Kwon, Y. Zorlu, B. Cosut, H. Kim, A. Facchetti, C. Kim, Hakan Usta, Solution-processable BODIPY-based small molecules for semiconducting microfibers in organic thin-film transistors, ACS Appl. Mater. Interfaces 8 (2016) 14077–14087, https://doi.org/10.1021/acsami.6b02788.

[24] A. Pudo, J. Ortyl, I. Kamińska. Proceedings of 18th int. Electr.. Conf. Synth. Org. Chem., 2014, pp. 1–7.

[25] R. Arcos-Ramos, M. Maldonado-Domínguez, J. Ordóñez-Hernández, M. Romero-Ávila, N. Farfán, M.P. Carreón-Castro, 3-Substituted-7-(diethylamino) coumarins as molecular scaffolds for the bottom-up self-assembly of solids with extensive p-stacking, J. Mol. Struct. 1130 (2016) 914–921, https://doi.org/10.1016/j.molstruc.2016.10.080.

[26] A.Y. Bochkov, I.O. Akchurin, O.A. Dyachenko, V.F. Traven, NIR-fluorescent coumarin-fused BODIPY dyes with large Stokes shifts, Chem. Commun. 49 (2013) 11653–11655, https://doi.org/10.1039/C3CC46498A.

[27] I. Esnal, G. Duran-Sampedro, A.R. Agarrabeitia, J. Bañuelos, I. García-Moreno, M.A. Macías, E. Peña-Cabrera, I. López-Arbeloa, S. de la Moya, M.J. Ortiz, Coumarin–BODIPY hybrids by heteroatom linkage: versatile, tunable and photostable dye lasers for UV irradiation, J. Phys. Chem. Chem. Phys. 17 (2015) 8239–8247, https://doi.org/10.1039/C5CP00193E.

[28] Y. Bai, X. Shi, Y. Chen, C. Zhu, Y. Jiao, Z. Han, W. He, Z. Guo, Coumarin/BODIPY hybridisation for ratiometric sensing of intracellular polarity oscillation, Chem. Eur J. 24 (2018) 7513–7524, https://doi.org/10.1002/chem.201800915.

[29] Y. Qian, B. Yang, Y. Shen, Q. Du, L. Lin, J. Lin, H. Zhu, A BODIPY–coumarin-based selective fluorescent probe for rapidly detecting hydrogen sulfide in blood plasma and living cells, Sens. Actuators, B 182 (2013) 498–503, https://doi.org/10.1016/j.snb.2013.03.031.

[30] J. Kang, F. Huo, Y. Zhang, J. Chao, R.M. Strongin, C. Yin, Detecting intracellular ClO- with ratiometric fluorescent signal and its application invivo, Sens. Actuators, B 273 (2018) 1532–1538, https://doi.org/10.1016/j.snb.2018.07.072.

[31] X. Liu, S. Zhan, Z. Hu, X. A ratio-metric fluorescent sensor design platform with red emission of Europium(III) as built-in fluorescence correction, Zhang, Tetrahedron Lett. 60 (2019) 1607–1610, https://doi.org/10.1016/j.tetlet.2019.05.027.

[32] L. Sansalone, S. Tang, J. Garcia-Amorós, Y. Zhang, S. Nonell, J.D. Baker, B. Captain, F.M. Raymo, A photoactivatable far-red/near-infrared BODIPY to monitor cellular dynamics in vivo, ACS Sens. 3 (2018) 1347–1353, https://doi.org/10.1021/acssensors.8b00262.

[33] H. Lee, Z. Yang, Y. Wi, T.W. Kim, P. Verwilst, Y.H. Lee, G. Han, C. Kang, J.S. Kim, BODIPY–Coumarin conjugate as an endoplasmic reticulum membrane fluidity sensor and its application to ER stress models, Bioconjugate Chem. 26 (2015) 2474–2480, https://doi.org/10.1021/acs.bioconjchem.5b00508.

[34] R. Corona-Sánchez, R. Arcos-Ramos, M. Maldonado-Domínguez, O. Amelines-Sarria, A. Jerezano-Domínguez, H. García-Ortega, M. Rivera-Hernández, M. P. Carreón-Castro, N. Farfán, Structural and morphological studies of meso-ethylcarbazole F-BODIPY thin films, Monat. Chem. 147 (2016) 1915–1923, https://doi.org/10.1007/s00706-016-1760-4.

[35] J. Ordoñez-Hernández, A. Jiménez-Sánchez, H. García-Ortega, N. Sánchez-Puig, M. Flores-Álamo, R. Santillan, N. Farfán, A series of dual-responsive Coumarin-Bodipy probes for local microviscosity monitoring, Dyes Pigments 157 (2018) 305–315, https://doi.org/10.1016/j.dyepig.2018.05.009.

[36] J.E. Hein, V.V. Fokin, Copper-catalyzed azide–alkynecycloaddition (CuAAC) and beyond: new reactivity of copper(i) acetylides, Chem. Soc. Rev. 39 (2010) 1302–1315, https://doi.org/10.1039/B904091A.

[37] B. Shen, Y. Qian, Click synthesis, Hg2+ sensor and Intramolecular fluorescence resonance energy transfer in novel BODIPY dendrons, Sens. Actuators, B 239 (2017) 226–234, https://doi.org/10.1016/j.snb.2016.08.004.

[38] R.S. Singh, R.K. Gupta, R.P. Paitandi, A. Misra, S. Pandey, Triazole-appended BODIPY–piperazine conjugates and their efficacy toward mercury sensing, New J. Chem. 39 (2015) 2233–2239, https://doi.org/10.1039/C4NJ01625D.

[39] A.N. Kursunlu, E. Guler, Novel fluorescent sensor for silver (I) based on the 3,4-bis-triazole Bodipy via dual-click chemistry, J. Mol. Struct. 1134 (2017) 345–349, https://doi.org/10.1016/j.molstruc.2017.01.003.

[40] A.C. Schulz-Fincke, M. Blaut, A. Braune, M. Gütschow, A BODIPY-tagged phosphono peptide as activity-based probe for human leukocyte elastase, ACS Med. Chem. Lett. 9 (2018) 345–350, https://doi.org/10.1021/acsmedchemlett.7b00533.

[41] M.R. Topka, P. H Dinolfo, Synthesis, characterization, and fluorescence properties of mixed molecular multilayer films of BODIPY and Zn(II) tetraphenylporphyrins, ACS Appl. Mater. Interfaces 7 (2015) 8053–8060, https://doi.org/10.1021/acsami.5b00519.

[42] J.J. Shie, Y.C. Liu, Y.M. Lee, C. Lim, J.M. Fang, C.H. Wong, An azido-BODIPY probe for glycosylation: initiation of strong fluorescence upon triazole formation, J. Am. Chem. Soc. 136 (2014) 9953–9961, https://doi.org/10.1021/ja5010174.

[43] K. Sivakumar, F. Xie, B.M. Cash, S. Long, H.N. Barnhill, Q. Wang, A fluorogenic 1,3-dipolar cycloaddition reaction of 3-azidocoumarins and acetylenes, Org. Lett. 6 (2004) 4603–4606, https://doi.org/10.1021/ol047955x.

[44] T. Hirano, H. Kubo, T. Shiraishi, K. Hiromoto, T. Fujiwara, H. Kagechika, Fluorescent properties of coumarins with dual functions constructed by two sequential reactions, Tetrahedron Lett. 53 (2012) 5916–5919, https://doi.org/10.1016/j.tetlet.2012.08.085.

[45] J.E. de la Cerda-Pedro, R. Arcos-Ramos, M. Maldonado-Domínguez, S. Rojas-Lima, M. Romero-Ávila, M.P. Carreón-Castro, R. Santillan, N. Farfán, H. López-Ruiz, Engineering organic semiconducting solids, Multicomponent access to crystalline 3-(4-aryl-1,2,3-triazolyl)coumarins, CrystEngComm 18 (2016), https://doi.org/10.1039/c6ce01041e, 5562-557.

[46] Ý.L. Du, Ý. Ni, M. Li, B. Wang, A fluorescent hydrogen peroxide probe based on a 'click' modified coumarin fluorophore, Tetrahedron Lett. 51 (2010) 1152–1154, https://doi.org/10.1016/j.tetlet.2009.12.049.

[47] Y. Huang, C. Zhang, Z. Xi, L. Yi, Synthesis and characterizations of a highly sensitive and selective fluorescent probe for hydrogen sulfide, Tetrahedron Lett. 57 (2016) 1187–1191, https://doi.org/10.1016/j.tetlet.2016.02.017.

[48] D. Kushwaha, R.P. Singh, V.K. Tiwari, Fluorogenic dual click derived bis-glycoconjugated triazolocoumarins for selective recognition of Cu (II) ion, Tetrahedron Lett. 55 (2014) 4532–4536, https://doi.org/10.1016/j.tetlet.2014.06.052.

[49] A.S. Kumar, I. Parveen, N. Ahmed, Highly selective and sensitive coumarin–triazole-based fluorometric 'turn-off' sensor for detection of Pb2+ ions, Luminescence 33 (2018) 713–721, https://doi.org/10.1002/bio.3468.

[50] Y. Zhou, K. Liu, J.Y. Li, Y. Fang, T.C. Zhao, C. Yao, Visualization of nitroxyl in living cells by a chelated copper(II) coumarin complex, Org. Lett. 13 (2011) 1290–1293, https://doi.org/10.1021/ol103077q.

[51] J.E. de la Cerda-Pedro, O.J. Hernández-Ortiz, R.A. Vázquez-García, H. López-Ruiz, R. Gómez-Aguilar, N. Farfán, I.I. Padilla-Martínez, 3-(4-Formylphenyl)-triazole functionalized coumarins as violet-blue luminophores and n-type semiconductors: synthesis, photophysical, electrochemical and thermal properties, RSC Adv. 12 (2022) 28137–28146, https://doi.org/10.1039/D2RA03266J.

[52] R.W. Wagner, J.S. Lindsey, Boron-dipyrromethene dyes for incorporation in synthetic multi-pigment light-harvesting arrays, Pure Appl. Chem. 68 (1996) 1373–1380, https://doi.org/10.1351/pac199668071373.

[53] H.L. Lin, W.C. Huang, Y.C. Chen, H.H. Chou, C.Y. Hsu, J.T. Lin, H.W. Lin, BODIPY dyes with β-conjugation and their applications for high-efficiency inverted small molecule solar cells, Chem. Comun. 48 (2012) 8913, https://doi.org/10.1039/C2CC34286C.

[54] Bruker. SAINT v8.37A, Bruker AXS Inc, Madison, WI, USA, 2015.

[55] R.H. Blessing, An empirical correction for absorption anisotropy, Acta Crystallogr. A51 (1995) 33–38, https://doi.org/10.1107/S0108767394005726.

[56] G.M. Sheldrick, A short history of SHELX, Acta Crystallogr. A64 (2008) 112–122, https://doi.org/10.1107/S0108767307043930.

[57] L.J. Farrugia, WinGX and ORTEP for windows: an update, J. Appl. Crystallogr. 45 (2012) 849–854, https://doi.org/10.1107/S0021889812029111.

[58] A.L. Spek, Structure validation in chemical crystallography, Acta Crystallogr. D65 (2009) 148–155, https://doi.org/10.1107/S090744490804362X.

[59] C.F. Macrae, I.J. Bruno, J.A. Chisholm, P.R. Edgington, P. McCabe, E. Pidcock, L. Rodriguez-Monge, R. Taylor, J. van de Streek, P.A. Wood, Mercury–CSD –.0 - new features for the visualization and investigation of crystal structures, J. Appl. Crystallogr. 41 (2008) 466–470, https://doi.org/10.1107/S0021889807067908.

[60] C.F. Mackenzie, P.R. Spackman, D. Jayatilaka, M.A. Spackman, Towards quantitative analysis of intermolecular interactions with Hirshfeld surfaces, IUCrJ 4 (2017) 575, https://doi.org/10.1039/B704980C.

[61] J.J. McKinnon, D. Jayatilaka, M.A. Spackman, Chem. Commun. (2007) 3814.

[62] Gaussian 09, Revision A.02, M.J. Frisch, G.W. Trucks, H.B. Schlegel, G.E. Scuseria, M.A. Robb, J.R. Cheeseman, G. Scalmani, V. Barone, B. Mennucci, G. A. Petersson, H. Nakatsuji, M. Caricato, X. Li, H.P. Hratchian, A.F. Izmaylov, J. Bloino, G. Zheng, J.L. Sonnenberg, M. Hada, M. Ehara, K. Toyota, R. Fukuda, J. Hasegawa, M. Ishida, T. Nakajima, Y. Honda, O. Kitao, H. Nakai, T. Vreven, J.A. Montgomery Jr., J.E. Peralta, F. Ogliaro, M. Bearpark, J.J. Heyd, E. Brothers, K.N. Kudin, V.N. Staroverov, R. Kobayashi, J. Normand, K. Raghavachari, A. Rendell, J.C. Burant, S.S. Iyengar, J. Tomasi, M. Cossi, N. Rega, J. M. Millam, M. Klene, J.E. Knox, J.B. Cross, V. Bakken, C. Adamo, J. Jaramillo, R. Gomperts, R.E. Stratmann, O. Yazyev, A.J. Austin, R. Cammi, C. Pomelli, J. W. Ochterski, R.L. Martin, K. Morokuma, V.G. Zakrzewski, G.A. Voth, P. Salvador, J.J. Dannenberg, S. Dapprich, A.D. Daniels, O. Farkas, J.B. Foresman, J. V. Ortiz, J. Cioslowski, D.J. Fox, Gaussian, inc, Wallingford CT (2009).

[63] A. Hasija, R. Bhowal, D. Chopra, Quantitative investigation of weak intermolecular interactions of −F and $-CF_3$ substituted in situ cryocrystallized benzaldehydes, Cryst. Growth Des. 20 (2020) 7921, https://doi.org/10.1021/acs.cgd.0c01196.

[64] A. Gavezzotti, Calculation of intermolecular interaction energies by direct numerical integration over electron densities. 2. An improved polarization model and the evaluation of dispersion and repulsion energies, J. Phys. Chem. B 107 (2003) 2344, https://doi.org/10.1021/jp022288f.

[65] C. Espinosa-González, I. Moggio, E. Arias-Marín, J. Romero-García, R. Cruz-Silva, J. Le Moignec, J. Ortiz-Cisneros, Layer-by-layer assembled films of a rigid poly(phenyl-ethynylene) and alternate poly(phenyl-ethynylene)/poly(aniline), Synthetic Materials 139 (2003) 155–161, https://doi.org/10.1016/S0379-6779(03)00121-8.

[66] F.T.L. Muniz, M.A.R. Miranda, C. Morilla dos Santos, J.M. Sasaki, The Scherrer equation and the dynamical theory of X-ray diffraction, Acta Crystallogr. A72 (2016) 385–390, https://doi.org/10.1107/S205327331600365X.

[67] C. Adamo, D. Jacquemin, The calculations of excited-state properties with time-dependent density functional theory, Chem. Soc. Rev. 42 (2013) 845–856, https://doi.org/10.1039/C2CS35394F.

[68] M. Cossi, N. Rega, G. Scalmani, V. Barone, Energies, structures, and electronic properties of molecules in solution with the C-PCM solvation model, J. Comput. Chem. 24 (2003) 669–681, https://doi.org/10.1002/jcc.10189.

[69] C.M. Cardona, W. Li, A.E. Kaifer, D. Stockdale, G.C. Bazan, Electrochemical considerations for determining absolute frontier orbital energy levels of conjugated polymers for solar cell applications, Adv. Mater. 23 (2011) 2367–2371, https://doi.org/10.1002/adma.201004554.

[70] J. Sworakowski, How accurate are energies of HOMO and LUMO levels in small-molecule organic semiconductors determined from cyclic voltammetry or optical spectroscopy? Synth. Met. 235 (2018) 125–130, https://doi.org/10.1016/j.synthmet.2017.11.013.

[71] Haldor-Topsoe, Geometric Factors in Four-point Resistivity Measurement Semiconductor Division, 1986.

[72] G. Allen, J.C. Bevington (Eds.), Comprehensive Polymer Science and Supplements Reference Work, Pergamon Press, 1996.

[73] M.A. Aegerter, M. Mennig (Eds.), Sol-gel Technologies for Glass Producers and Users, Springer Science and Business Media, LLC, 2004, https://doi.org/10.1007/978-0-387-88953-5.

[74] H.-L. Kee, C. Kirmaier, L. Yu, P. Thamyongkit, W.J. Youngblood, M.E. Calder, L. Ramos, B.C. Noll, D.F. Bocian, W.R. Scheidt, R.R. Birge, J.S. Lindsey, D. Holten, Structural control of the photodynamics of boron-dipyrrin complexes, J. Phys. Chem. B 109 (2005) 20433–20443.

[75] M. Farfán-Paredes, O. González-Antonio, D.E. Tahuilan-Anguiano, J. Peón, A. Ariza, P.G. Lacroix, R. Santillan, N. Farfán, Physicochemical and computational insight of ^{19}F NMR and emission properties of meso-(o-aryl)-BODIPYs, New J. Chem. 44 (2020), 19459, https://doi.org/10.1039/D0NJ02576C.

[76] E.V. García-Báez, F.J. Martínez-Martínez, H. Höpfl, I.I. Padilla-Martinez, π-Stacking interactions and C-H···X (X = O, aryl) hydrogen bonding as directing features of the supramolecular self-association in 3-carboxy and 3-amido coumarin derivatives, Cryst. Growth Des. 3 (2003) 35–45, https://doi.org/10.1021/cg0255826.

[77] A. Rose, S.V. Kumar, S. Swavey, J. Erb, A simple and efficient protocol for screening boron-dipyrromethene dyes using TD-DFT and an examination of the aryl-meso position, Comput. Theor. Chem. 1118 (2017) 107–114, https://doi.org/10.1016/j.comptc.2017.08.029.

[78] F.H. Allen, C.A. Baalham, J.P.M. Lommerse, P.R. Raithby, Carbonyl–carbonyl interactions can be competitive with hydrogen bonds, Acta Crystallogr., Sect. B: Struct. Sci. B54 (1998) 320–329, https://doi.org/10.1107/S0108768198000146.

[79] P.G. Lacroix, I.I. Padilla-Martinez, H. Lopez-Sandoval, K. Nakatani, Through space charge transfer and quadratic nonlinear optical (NLO) properties in alternated stacks of 2-amino-1,3-benzothiazole–ethylcoumarin-3-carboxylate charge transfer complexes: from the molecular to the bulk NLO response, New J. Chem. 28 (2004) 542–547, https://doi.org/10.1039/B313294C.

[80] C. Wang, H. Dong, L. Jiang, W. Hu, Organic semiconductor crystal, Chem. Soc. Rev. 47 (2018) 422–450, https://doi.org/10.1039/C7CS00490G.

[81] M. Paramasivam, S. Kanvah, Rational tuning of AIEE active coumarin based α-cyanostilbenes toward far-red/NIR region using different π-spacer and acceptor units, J. Phys. Chem. C 120 (2016) 10757–10769, https://doi.org/10.1021/acs.jpcc.6b01334.

[82] A. Orte, E. Debroye, M.J. Ruedas-Rama, E. Garcia-Fernandez, D. Robinson, L. Crovetto, E.M. Talavera, J.M. Alvarez-Pez, V. Leen, B. Verbelen, L.C.D. de Rezende, W. Dehaen, J. Hofkens, M.V. der Auweraer, N. Boens, Effect of the substitution position (2, 3 or 8) on the spectroscopic and photophysical properties of BODIPY dyes with a phenyl, styryl or phenylethynyl group, RSC Adv. 6 (2016), 102899, https://doi.org/10.1039/C6RA22340K.

[83] R. Hu, E. Lager, A. Aguilar-Aguilar, J. Liu, J.W.Y. Lam, H.H.Y. Sung, I.D. Williams, Y. Zhong, K.S. Wong, E. Peña-Cabrera, B.Z. Tang, Twisted intramolecular charge transfer and aggregation-induced emission of BODIPY derivatives, J. Phys. Chem. C 113 (2009) 15845–15853, https://doi.org/10.1021/jp902962h.

[84] S. Chibani, A.D. Laurent, B. Le Guennic, D. Jacquemin, Improving the accuracy of excited-state simulations of BODIPY and aza-BODIPY dyes with a joint SOS-CIS(D) and TD-DFT approach, J. Chem. Theor. Comput. 10 (2014) 4574–4582, https://doi.org/10.1021/ct500655k.

[85] Y. Gawale, N. Sekar, Investigating the excited state optical properties and origin of large Stokes shift in Benz[c,d]indole N-Heteroarene BF_2 dyes with ab initio tools, J. Photochem. Photobiol. B Biol. 178 (2018) 472–480, https://doi.org/10.1016/j.jphotobiol.2017.12.006.

[86] A.E. Pogonin, A.Y. Shagurin, M.A. Savenkova, F.Y. Telegin, Y.S. Marfin, A.S. Vashurin, Quantum chemical study aimed at modeling efficient aza-BODIPY NIR dyes: molecular and electronic structure, absorption, and emission spectra, Molecules 25 (2020) 5361, https://doi.org/10.3390/molecules25225361.

[87] M. Laine, N.A. Barbosa, R. Wieczorek, M.Y. Melnikov, A. Filarowski, Calculations of BODIPY dyes in the ground and excited states using the M06-2X and PBE0 functionals, J. Mol. Model. 22 (2016) 260.

[88] Q. Zhang, L. Li, Photodynamic combinational therapy in cancer treatment, J. B.U.ON 23 (2018) 561–567, https://doi.org/10.1016/j.pdpdt.2018.06.002.

[89] A. Bodaghi, H.R. Shamlouei, Design and TDDFT study of the novel structures similar to BODIPY with prominent fluorescence properties, Int. J. New Chem. 9 (2019) 36–52.

[90] H. Nakayama, S. Kimura, Suppression of HOMO–LUMO transition in a twist form of oligo (phenyleneethynylene) clamped by a right-handed helical peptide, J. Phys. Chem. A 115 (2011) 8960–8968, https://doi.org/10.1021/jp200997c.

[91] Y. Kato, H. Matsumoto, T. Mori, Absence of HOMO/LUMO transition in charge-transfer complexes of thienoacenes, J. Phys. Chem. A 125 (2021) 146–153, https://doi.org/10.1021/acs.jpca.0c08925.

[92] P. Kimber, F. Plasser, Energy component analysis for electronically excited states of molecules: why the lowest excited state is not always the HOMO/LUMO transition, J. Chem. Theor. Comput. 19 (2023) 2340–2352, https://doi.org/10.1021/acs.jctc.3c00125.

[93] C.A. Franca, A.C. González Baró, R. Pis Diez, Theoretical study and vibrational spectroscopy of two 5,6,7-trioxygenated coumarins, J. Mol. Struct. 843 (2007) 57–65, https://doi.org/10.1016/j.molstruc.2006.12.035.

[94] L. Han, R. Kang, X. Zu, Y. Cui, J. Gao, Novel coumarin sensitizers based on 2-(thiophen-2-yl)thiazole π-bridge for dye-sensitized solar cells, Photochem. Photobiol. Sci. 14 (2015) 2046–2053, https://doi.org/10.1039/c5pp00216h.

[95] A. Cisse, M. Djande, Capo-Chichi, A. Khonté, J.P. Bakhoum, F. Delattre, J. Yoda, A. Saba, A. Tine, J.J. Aaron, Quantitative study of the substituent effects on the electronic absorption and fluorescence spectra of coumarins, J. Phys. Org. Chem. 33 (2020), e4014, https://doi.org/10.1002/poc.4014.

[96] S. Canola, F. Negri, Role of the HOMO-1 orbital on the p-type charge transport of the fused-ring thienoacene DBTDT, J. Phys. Chem. C 119 (2015) 11499–11505, https://doi.org/10.1021/acs.jpcc.5b02713.

[97] A. Rose, S.V. Kumar, S. Swavey, J. Erb, A simple and efficient protocol for screening boron-dipyrromethene dyes using TD-DFT and an examination of the aryl-meso position, Computational and Theoretical Chemistry 1118 (2017) 107–114, https://doi.org/10.1016/j.comptc.2017.08.029.

[98] R. Misra, Tuning of second-order nonlinear optical response properties of aryl-substituted boron-dipyrromethene dyes: unidirectional charge transfer coupled with structural tailoring, J. Phys. Chem. C 121 (2017) 5731–5739, https://doi.org/10.1021/acs.jpcc.6b13035.

[99] J. Songkhao, R. Banerjee, S. Debnath, S. Narasimhan, N. Wannaprom, P. Vanalabhpatana, N. Seriani, R. Gebauer, P. Thamyongkit, Structure-property relationship of π-extended boron-dipyrromethene derivatives towards optoelectronic applications, Dyes Pigments 142 (2017) 558e57, https://doi.org/10.1016/j.dyepig.2017.03.050.

[100] T. Johansson, W. Mammo, M. Svensson, M.R. Andersson, O. Inganäs, Electrochemical bandgaps of substituted polythiophenes, J. Mater. Chem. 13 (2003) 1316–1323, https://doi.org/10.1039/B301403G.

[101] D. Gupta, Y. Hong, Understanding the effect of semiconductor thickness on device characteristics in organic thin film transistors by way of two-dimensional simulations, Org. Electron. 11 (2010) 127–136, https://doi.org/10.1016/j.orgel.2009.10.009.

[102] I. Torres-Moya, I. Arrechea-Marcos, C. Tardío, J.R. Carrillo, A. Díaz-Ortiz, J.T. Lopez Navarrete, M.C. Ruiz-Delgado, P. Prieto, R. Ponce-Ortiz, D–A–D 2H-benzo[d][1,2,3]triazole derivatives as p-type semiconductors in organic field-effect transistors, RSC Adv. 8 (2018) 21879–21888, https://doi.org/10.1039/C8RA03246G.

[103] S. Singh, V. Venugopalan, K. Krishnamoorthy, Organic soluble and uniform film forming oligoethylene glycol substituted BODIPY small molecules with improved hole mobility, Phys. Chem. Chem. Phys. 16 (2014) 13376–13382, https://doi.org/10.1039/C4CP01098A.

[104] S. Wanwong, P. Khomein, S. Thayumanavan, BODIPY dyads and triads: synthesis, optical, electrochemical and transistor properties, Chem. Cent. J. 12 (2018) 60, https://doi.org/10.1186/s13065-018-0430-5.

[105] D. Liang, J. Li, S. Cui, J. Ma, M. Liu, C. Miao, P. Vivo, W. Yang, H. Zhang, Isoindigo-based aza-BODIPY small molecule for N-type organic field-effect transistors, Dyes Pigments 208 (2022), 110743, https://doi.org/10.1016/j.dyepig.2022.110743.

[106] B. Liu, J. Li, W. Yang, H. Yan, X. Gao, Q. Zhang, Naphthalene imide derived BODIPY analogues as n-channel semiconductors, Dyes Pigments 199 (2022), 110053, https://doi.org/10.1016/j.dyepig.2021.110053.